



TECHNISCHE
UNIVERSITÄT
WIEN

Diploma Thesis

Influence of Mo on the structure and fracture-mechanical properties of TiB_{2+z} thin films

carried out for the purpose of obtaining the degree of Dipl.-Ing.

under the supervision of

Ass. Prof. Dr. techn. Helmut Riedl-Tragenreif

and

Dipl.-Ing Christoph Fuger

Institute of Materials Science and Technology, E308

submitted at TU Wien

Faculty of Mechanical and Industrial Engineering

by

Anna Viktoria Hirle, BSc

11741773

Am Spitz8/13

1210 Wien

Vienna, May 2022

*“Ever tried.
Ever failed.
No matter.
Try again.
Fail again.
Fail better.”*

-Samuel Beckett

This work was supported by Plansee Composite Materials GmbH and
Oerlikon Balzers Surface Solutions AG in the framework of the Christian Doppler
Laboratory for Surface Engineering of High-Performance Components

Affidavit

I declare in lieu of oath, that I wrote this thesis and performed the associated research
myself, using only literature cited in this volume.

Date

Signature

Acknowledgements

First, I want to express my appreciation for the chance I was given to work in such an incredible group. In the last two years I got the possibility to learn and work on something completely different than I did before. All the challenges, achievements, fun and laughter wouldn't have been the same without you!

My biggest THANKS goes to **Assistant Prof. Dipl.-Ing. Dr.techn. Helmut Riedl-Tragenreif** and **Projektass. Dipl.-Ing. Christoph Fuger** for giving me this project to work on. Without your amazing supervision, constant motivation and support that thesis would have never been possible. Also, I am immensely grateful for the constant help and knowledge input I received from **Projektass. Dipl.-Ing. Dr.techn. Rainer Hahn**.

Lukas Zauner and **Philipp Ertelthaler** without you it would have been impossible to finish or even start the coatings for this thesis. Thank you for the many hours you spent helping me repairing Heidi and Noreia. Todes Danke! **Sophie**, I cannot thank you enough for being my partner in crime, especially these last few weeks. I am super excited to see, what the next three years will bring for us! **Alex, Oliver, Stefan, Ahmed, Thomas, Tomasz, Philip**, and the **Rest** of the group, thank you for welcoming me to the team and your willingness to support me, whenever needed.

Furthermore, I want to thank **Szilárd Kolozsvári** and **Peter Polcik** from Plansee Composite Materials GmbH as well as **Oliver Hunold** and **Stephan Moser** from Oerlikon Surface Solutions AG for the possibility of getting an insight into their companies and the chance to carry out part of my experiments there.

Finally, I want to express my deepest gratitude to my family and friends. **Mama, Papa** and **Fini**, your unconditional love and encouragement are only two reasons, why I made it this far. **Alisa, Caro, Theri, Maria, Theresa, Sebastian, and Yannik**, I can't wish for better friends at home and in Vienna. Thank you, for always supporting me with food, hugs, and motivational words.

Table of Contents

Acknowledgements	iii
Table of Contents	iv
List of Figures	vi
Abstract	1
Kurzfassung	3
1. Introduction and Motivation	5
1.1 Research interest in surface modification	5
1.2 Erosion and Solid Particle Erosion.....	6
2. Physical Vapor Deposition (PVD)	10
2.1 DC Sputtering.....	10
2.2 Direct Current Magnetron Sputtering (DCMS)	12
2.3 Thin film growth	13
3. Transition Metal Diborides	17
3.1 Ti - B System.....	19
3.2 Mo - B System.....	20
3.3 Ternary System Ti-Mo-B – Mo alloying	22
4. Coating Synthesis	24
5. Characterization Techniques	25
5.1 Scanning Electron Microscopy (SEM)	25
5.2 Transmission Electron Microscopy.....	26
5.3 Nanoindentation	27
5.4 X-ray Diffraction Analysis (XRD).....	29
5.5 Micromechanical Testing.....	31
5.6 Solid Particle Erosion Test ASTM G76.....	34
5.7 Further Techniques.....	35
6. Results and Discussion	36
6.1 Preliminary depositions.....	36
6.1.1 Structure and Morphology	38
6.1.2 Mechanical Properties	40
6.2 Detailed Investigation of $TiB_{3.1}$, $Ti_{0.94}Mo_{0.06}B_{1.94}$ and $Ti_{0.88}Mo_{0.12}B_{1.59}$ thin films..	41
6.2.1 Structure and Morphology	41
6.2.2 Mechanical Properties	46
6.2.3 Fracture Toughness	48

6.2.4 Erosion tests	49
6.2.5 Thermal Properties	52
7. Conclusions	54
Appendix A	ix
Literature	xi

List of Figures

Figure 1: Schematic of the basic tribological system- Adapted from [25]	7
Figure 2: Correlation between impact angle and amount of erosion for a) Ductile behavior and b) Brittle behavior. Adapted from [2].....	8
Figure 3: DC magnetron sputter configuration and principle of target sputtering of a PVD system. Figure was adapted from [40]	12
Figure 4: Schematic of the three modes of thin film growth: a) Volmer-Weber (Island), b) Frank-Van der Merwe (Layer-by-layer), and c) Stranski-Krastanov (Layer plus Island). Adapted from [4].....	14
Figure 5: SZM by Thornton. Taken from [4].....	15
Figure 6: Structure zone diagram by Anders [42].....	16
Figure 7: Overview of group IV to VI TMB ₂ with corresponding melting points and preferred structure.....	17
Figure 8: Schematics of the α -AlB ₂ structure (space group 191, hexagonal P6/mmm). The black spheres symbolize B and the blue spheres the M atoms.....	18
Figure 9: Binary Ti-B phase diagram. Taken from [51]	19
Figure 10: Binary Mo-B phase diagram. Taken from [57].	20
Figure 11: Poisson's ratio over the G/B ratio for the two binary systems TiB ₂ and MoB ₂ , as well as different ternary compositions of the Ti _{1-x} Mo _x B _{2±z} system.	22
Figure 12: Results of DFT calculations for the energy of formation E _f for different scenarios of Mo incorporation into the crystal lattice: Metal substitutional, Boron substitutional, and Boron plane interstitial. B atoms are shown in green, Mo in violet and Ti in blue.	23
Figure 13: Typical load-displacement curve derived from nanoindentation. With P _{max} (peak load), h _{max} (max. displacement) and S (initial unloading contact stiffness) being the most important values. Adapted from [65]	27
Figure 14: Schematic of X-ray diffraction on a crystal plane (Bragg's Law). Adapted from [68]	29
Figure 15 Image of a micro-cantilever and relevant geometrical information (l=length of the cantilever, w=film thickness, a=initial crack length and b=cantilever width)	32
Figure 16 DUCOM Air Jet Erosion Tester	34
Figure 17: The progression of Ti and B over the Mo content within the deposited coatings a). The influence of Mo on the boron to metal (B/M) ratio is shown in b).....	37

Figure 18: SEM fracture cross sections on Si substrates. All images were obtained using 10 kV voltage (FEGSEM Quanta 250); a) corresponds to coating $TiB_{3.1}$, b) to coating $Ti_{0.96}Mo_{0.04}B_{2.21}$ c) to coating $Ti_{0.94}Mo_{0.06}B_{1.94}$, d) to coating $Ti_{0.90}Mo_{0.10}B_{1.95}$, e) to coating $Ti_{0.88}Mo_{0.12}B_{1.59}$, f) to coating $Ti_{0.79}Mo_{0.21}B_{1.65}$ and g) to coating $Ti_{0.71}Mo_{0.29}B_{0.8}$ 38

Figure 19: X-ray diffractograms of the deposited thin films with increasing Mo content from top to bottom. Indicated in orange are the reference positions of α - TiB_2 peaks and the reference positions of α - MoB_2 peaks in dark red. 39

Figure 20: The mechanical properties hardness (H) and indentation modulus (E) are plotted over the Mo content. Hardness values are indicated by the blue boxes, and the values for the indentation modulus by the pink triangles. 40

Figure 21 SEM images on Al_2O_3 substrate, cross sections, a) $TiB_{3.1}$, b) $Ti_{0.94}Mo_{0.06}B_{1.94}$ c) $Ti_{0.88}Mo_{0.12}B_{1.59}$ 41

Figure 22 TEM images $TiB_{3.1}$, a) overview, b) bright field close to surface, c) bright field close to substrate, d) SAED close to the surface, and e) SAED close to the substrate 42

Figure 23: TEM images $Ti_{0.94}Mo_{0.06}B_{1.94}$, a) overview, b) bright field close to surface, c) bright field close to substrate d) SAED close to surface, e) SAED close to the substrate 43

Figure 24: TEM images $Ti_{0.88}Mo_{0.12}B_{1.59}$, a) overview, b) bright field close to surface, c) bright field close to substrate d) SAED close to surface, e) SAED close to substrate..... 44

Figure 25: XRD diffractogram of the three coating systems, measured on austenite substrates and the reference diffractograms of the used targets for the Mo containing coatings. The reference pattern for the austenite substrate is indicated by light grey symbols, α - TiB_2 in orange, α - MoB_2 in dark red, t- MoB (tetragonal) in violet, and o- MoB (orthorhombic) in light red. 45

Figure 26: Mechanical properties plotted over the Mo content. a) Hardness H in blue, Indentation modulus E in pink, b) H^3/E^2 ratio in light orange 46

Figure 27: a) Fracture toughness over Mo content and b-d) the fracture cross-sections 48

Figure 28: Progression of SPE at 30° for a) $TiB_{3.1}$, b) $Ti_{0.94}Mo_{0.06}B_{1.94}$ and c) $Ti_{0.88}Mo_{0.12}B_{1.59}$ 50

Figure 29: Mass loss in mg over time during erosion experiments at impact angle 30° for the uncoated substrate $TiAl6V4$ (grey stars), $TiB_{3.1}$ (blue circles) and the Mo containing thin films pink boxes and green triangles 51

Figure 30: Resulting XRD diffractograms for the 10 h annealing of $TiB_{3.1}$ in the as deposited state and after the annealing at 500, 600, 700 and 800 °C. 52

Figure 31: Resulting XRD diffractograms for the 10 h annealing of $\text{Ti}_{0.88}\text{Mo}_{0.12}\text{B}_{1.59}$ in the as deposited state and after the annealing at 500, 600, 700 and 800 °C..... 53

Figure 32: Resulting diffractograms of $\text{TiB}_{3.1}$ in the as deposited state and after annealing for 1 h at 500, 600, 700 and 800 °C ix

Figure 33: Resulting diffractograms of $\text{Ti}_{0.94}\text{Mo}_{0.06}\text{B}_{1.94}$ in the as deposited state and after annealing for 1 h at 500, 600, 700 and 800 °C ix

Figure 34: Resulting diffractograms of $\text{Ti}_{0.94}\text{Mo}_{0.06}\text{B}_{1.94}$ in the as deposited state and after annealing for 10 h at 500, 600, 700 and 800 °C x

Figure 35: Resulting diffractograms of $\text{Ti}_{0.88}\text{Mo}_{0.12}\text{B}_{1.59}$ in the as deposited state and after annealing for 10 h at 500, 600, 700 and 800 °C x

Abstract

Surface protection of highly stressed machine elements used in energy production, aviation, or the manufacturing industry is an important topic with respect to the sustainable usage of resources, especially for extending the longevity of high-performance components. For this purpose, transition metal diboride based coating materials increasingly come into the research focus. Titanium diboride has been intensively investigated and exhibits favorable characteristics, such as high hardness, Young's modulus, and a wide phase stability. Nevertheless, its inherent brittleness is highly disadvantageous. Different theoretical studies suggest novel alloying strategies – forming ternary $T\text{M}_I\text{T}\text{M}_{II}\text{B}_{2+z}$ – to reduce the limited fracture tolerance.

In detail, Density Functional Theory (DFT) calculations using the G/B ratio (Pugh criterion) as well as the Poisson's ratio (Frantsevich criterion) to quantify the brittle to ductile transition suggest the addition of Mo into TiB_2 to be highly promising. Therefore, in the present study, direct current magnetron sputtering is used to investigate the influence of Mo on the structure-mechanical properties of TiB_{2+z} thin films. TiB_2/C 99/1 mol%, TiB_2/MoB 95/5 mol%, TiB_2/MoB 90/10 mol%, and TiB_2/MoB 80/20 mol% powder metallurgical produced targets are applied for the deposition of $\text{Ti}_{1-x}\text{Mo}_x\text{B}_{2+z}$ coatings. $\text{TiB}_{3.1}$, $\text{Ti}_{0.94}\text{Mo}_{0.06}\text{B}_{1.94}$, and $\text{Ti}_{0.88}\text{Mo}_{0.12}\text{B}_{1.59}$ are investigated in more detail by a broad set of characterization techniques, i.e., X-ray diffraction (XRD), scanning, and transmission electron microscopy (SEM & TEM), as well as micro mechanical testing. Morphological analyses revealed fine-columnar films with a predominant α -structure (AlB_2 structure type, SG 191). An increasing amount of Mo is accompanied by a decreasing B content linked to enhanced scattering effects within the Mo containing plasma. Nanoindentation experiments exhibit super-hard $\text{TiB}_{3.1}$ with $H = 42.27 \pm 1.37$ GPa, decreasing with increasing Mo to $H = 39.18 \pm 1.34$ for $\text{Ti}_{0.94}\text{Mo}_{0.06}\text{B}_{1.94}$ and again slightly sinking to $H = 38.9 \pm 1.82$ GPa for $\text{Ti}_{0.88}\text{Mo}_{0.12}\text{B}_{1.59}$. The drop in hardness is attributed to the changing film texture and formation of sub-stoichiometric nano-crystalline domains (observed while TEM analysis). The indentation modulus is slightly decreasing from 516 ± 13 GPa for $\text{TiB}_{3.1}$ to 496 ± 33 GPa for the thin film containing the highest Mo content. The fracture toughness remains constant at around $3.0 \text{ MPa}\sqrt{\text{m}}$ for $\text{TiB}_{3.1}$ as well as $\text{Ti}_{0.94}\text{Mo}_{0.06}\text{B}_{1.94}$ but increases with higher Mo content to $3.25 \pm 0.34 \text{ MPa}\sqrt{\text{m}}$ ($\text{Ti}_{0.88}\text{Mo}_{0.12}\text{B}_{1.59}$), validating the theoretical predictions. Here, we need to mention that during DFT based calculations only the elastic constants for pure MoB_2 perfectly fulfill the semi-empirical ductile criteria. The phase

stability was evaluated during vacuum annealing at 500, 600, 700, and 800 °C for 1 and 10 h, whereby only $\text{Ti}_{0.88}\text{Mo}_{0.12}\text{B}_{1.59}$ revealed minor indications of $\alpha\text{-MoB}_2$ at 800 °C for 10 h.

In summary, the theoretically predicted positive effects of adding Mo into TiB_2 could be experimentally verified. Detailed structure-mechanical analyses revealed α -structured $\text{Ti}_{1-x}\text{Mo}_x\text{B}_{2\pm z}$ solid solutions, sustaining and even slightly enhancing the fracture-mechanical properties of this super-hard coating material.

Kurzfassung

Ein kontinuierlich steigender Bedarf an Mobilität und auch Energie bedingt den nachhaltigen Einsatz von Ressourcen und Komponenten. Eine wichtige Rolle in diesem vielschichtigen Technologie-Puzzle spielen Materialien und hier speziell ihre Oberflächen. Die gezielte Verbesserung von Materialeigenschaften durch Oberflächentechnik findet in diversen Industriebereichen Anwendung – Luftfahrttechnik, Transport- und Automobil-Industrie, oder auch Energieerzeugung. Beschichtungsmaterialien auf Basis von Übergangsmetall diboriden rücken zunehmend in den Fokus der Forschung und Industrie. Titandiborid, ein keramisches Material, das bereits intensiv erforscht wird, weist hervorragende thermische und mechanische Eigenschaften auf (z.B. hohe Härte oder Phasenstabilität). Von großem Nachteil ist die limitierte Duktilität von TiB_2 . Aus Basis von theoretischen Vorhersagen, wirkt sich die Bildung von ternären $Ti_I Ti_{II} B_{2+z}$ Legierungen positiv auf die Brucheigenschaften aus.

Dichtefunktionaltheorie (DFT) Berechnungen, bei denen das G/B-Verhältnis (Pugh-Kriterium) und die Poissonzahl (Frantsevich-Kriterium) zur Quantifizierung des Übergangs zwischen Sprödigkeit und Duktilität herangezogen wird, deuten darauf hin, dass das Zulegieren von Mo ein sehr vielversprechender Ansatz ist. Auf Basis dieser Vorhersage, werden im Zuge dieser Diplomarbeit die strukturmechanischen Eigenschaften von Mo legierten TiB_{2+z} Dünnschichten (DC-Magnetron-Sputtern) untersucht. Pulvermetallurgisch hergestellte TiB_2/C 99/1 mol%, TiB_2/MoB 95/5 mol%, TiB_2/MoB 90/10 mol% und TiB_2/MoB 80/20 mol% Targets werden für die Abscheidung ternärer $Ti_{1-x}Mo_xB_{2+z}$ -Schichten verwendet. Im Zuge einer Vorselektion werden $TiB_{3.1}$, $Ti_{0.94}Mo_{0.06}B_{1.94}$ und $Ti_{0.88}Mo_{0.12}B_{1.59}$ mit einer Reihe von hochauflösenden Charakterisierungstechniken wie Röntgenbeugung (XRD), Raster- und Transmissions-Elektronenmikroskopie (SEM & TEM) sowie mikro-mechanischer Tests im Detail untersucht. Morphologischen Untersuchungen zeigen eine fein-kolumnare Struktur der Schichten, sowie eine dominante α -Phase, AlB_2 -Strukturtyp (SG 191). Bei steigender Menge von zulegiertem Mo sinkt der B-Gehalt in den abgeschiedenen Schichten, was auf verstärkte Streueffekte innerhalb des Mo-haltigen Plasmas zurückzuführen ist. Die Analyse der mechanischen Eigenschaften mittels Nanoindentation ergeben für $TiB_{3.1}$ eine Härte von $H = 42.27 \pm 1.37$ GPa, (Superhärte), die mit zunehmendem Mo-Gehalt auf $H = 39.18 \pm 1.34$ für $Ti_{0.94}Mo_{0.06}B_{1.94}$ sinkt, wobei $Ti_{0.88}Mo_{0.12}B_{1.59}$ ($H = 38.9 \pm 1.82$ GPa) das untere Limit darstellt. Dieser geringe Härteabfall wird auf die veränderte Filmtextrur und die Bildung von substöchiometrisch, nanokristallinen Kristallite zurückgeführt (beurteilt mittels TEM-Analyse). Der E-Modul sinkt

in einem geringen Ausmaß mit steigendem Mo-Gehalt, von 516 ± 13 GPa für $\text{TiB}_{3.1}$ auf 496 ± 33 GPa für $\text{Ti}_{0.94}\text{Mo}_{0.06}\text{B}_{1.94}$. Die Bruchzähigkeit bleibt konstant bei etwa $3.0 \text{ MPa}\sqrt{\text{m}}$ für $\text{TiB}_{3.1}$ sowie $\text{Ti}_{0.94}\text{Mo}_{0.06}\text{B}_{1.94}$, steigt jedoch mit höherem Mo-Gehalt auf $3.25 \pm 0.34 \text{ MPa}\sqrt{\text{m}}$ ($\text{Ti}_{0.88}\text{Mo}_{0.12}\text{B}_{1.59}$) an. Dies bestätigt die theoretischen Vorhersagen. An dieser Stelle muss erwähnt werden, dass in den theoretischen DFT Berechnungen einzig reines MoB_2 die Kriterien für duktilen Verhalten erfüllt. Die Phasenstabilität wurde durch Vakuumglühen bei 500, 600, 700 und 800 °C für 1 sowie 10 Stunden untersucht. Eine Phasentransformation – im Detail die Bildung von geringen Mengen von $\alpha\text{-MoB}_2$ – konnte lediglich bei $\text{Ti}_{0.88}\text{Mo}_{0.12}\text{B}_{1.59}$ nach 10 h bei 800 °C festgestellt werden.

Zusammenfassend konnten die theoretisch vorhergesagten positiven Effekte einer Zugabe von Mo in TiB_2 experimentell verifiziert werden. Detaillierte strukturmechanische Analysen ergaben im untersuchten Legierungsbereich α -strukturierte $\text{Ti}_{1-x}\text{Mo}_x\text{B}_{2\pm z}$ -Mischkristalle, welche leicht verbesserte bruchmechanischen Eigenschaften dieses superharten Beschichtungsmaterials ergeben.

1. Introduction and Motivation

Behind every research stands an idea, followed by a theoretical review of feasibility. If successful, actual experiments in the laboratory will be conducted. However, the motivation for such a research project can originate from different points of view. The motivation behind the present work will be given in the following sections.

1.1 Research interest in surface modification

The requirements for modern technical applications concerning their reliability, service time, costs, and efficiency are still increasing, leading to a necessity for new and innovative ideas [1]. Component failures due to damage by solid particle erosion (SPE) are a severe problem for aircraft engines, wind turbines, and gas turbines for power generation [2]. Consequently, a big focus lies in the research and development of materials science, especially surface engineering. In particular, the modification of surfaces through the application of coatings with properties distinctly different from the ones of the bulk material has attracted attention in the last decades [3, 4]. Thin film technology reaches back to ancient times, often used for the craft of gold beating [5]. In modern times thin films have already reached widespread fields of applications as, for example, decorative films [3, 6], permeation barriers [6], and optical films [6], as well as for biotechnology and energy generation [5]. To prevent tools and components from corrosion, oxidation, wear, and erosion, thin films deposited by Physical Vapor Deposition (PVD) have been widely established [4]. PVD describes a collection of techniques for the deposition of thin solid films. The underlying principle of all these methods is the vaporization of material followed by transportation towards the substrate and subsequent condensation and growth [1].

For cutting tools, Titanium Nitride (TiN) was the first industrially used PVD coating, later by Titanium Aluminum Nitride (TiAlN), which is still an essential coating [7]. Other established coatings are CrN, AlCrN, and TiB₂. Apart from the already widely used nitride coatings, transition metal diborides (TMB₂) show promising characteristics [8]. Their high melting point (3000 °C), high hardness, elastic modulus, and chemical stability/inertness [9, 10] are properties that make them highly favorable for future applications as protective coatings. Within the scope of this work, one/two system/s were chosen due to their industrial relevance and their potential good properties.

Titanium Diboride (TiB₂), which was already studied extensively, is known as a protective coating - manufactured by Chemical Vapor Deposition (CVD) or magnetron sputtering - for

the machining of aluminum alloys [9] or as diffusion barriers [11]. Further industrial applications of TiB₂ - particularly protective coatings against wear and erosion - are promoted by its excellent properties such as a high hardness (up to 40 GPa), high melting point (3225 °C), and Young's modulus [12]. The significant disadvantages of TiB₂ are its low oxidation resistance and its inherent brittleness [13].

DFT calculations suggest that Mo alloying TiB₂ will increase the ductility of the material system. A ductile character is attributed to MoB₂ by DFT calculations [14]; however, the knowledge about MoB₂ PVD thin films is scarce. Sputtered MoB_{2-x} has shown a high hardness and hP3-MoB₂ (AlB₂-type) structure [15].

Ternary Diborides are as well rather uninvestigated. Nevertheless, few studies reported the effect of alloying elements on TMBs. Exemplary the systems W_{1-x}Ta_xB_{2-z} [16], W_{1-x}Al_xB_{2-z} [17], W_{1-x}V_xB_{2-z} [10], Ti_{1-x}Ta_xB_{2+Δ} [18] and Zr_{1-x}Ta_xB_y [19] are named here. Ternary systems, including Mo are scarce; here, Mo-Si-B is reported [20–22].

The following section will give the motivation for the present work viewed from an application-oriented point of view. Various causes trigger damage of materials/parts, e.g., in the tooling industry. Wear, and the associated erosion are important factors limiting the lifetime of a component. In order to increase the service life or prevent premature critical failure, coating with wear-resistant coatings is indicated.

1.2 Erosion and Solid Particle Erosion

Erosion is defined as the

“Progressive loss or damage to a solid surface caused by contact with a moving fluid. The fluid can be single phase or multi-phased, and the material removal can include a corrosion component.” [23]

Erosion is assigned to the field of tribology, an interdisciplinary science that deals with interacting surfaces in relative motion to each other (friction, wear, and lubrication under load) to keep damages as less as possible. A tribological system consists of a base body, a counterbody, the interfacial medium, the operating environment, and the relative motion and load acting on the system [24], schematically shown in **Figure 1**.

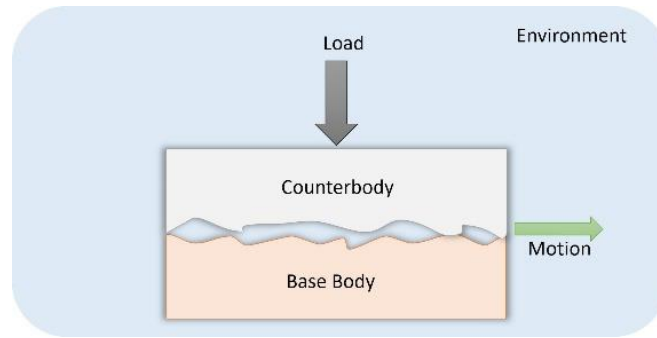


Figure 1.: Schematic of the basic tribological system-
Adapted from [25]

Wear is classified into different types and mechanisms. The four essential mechanisms are abrasive wear, adhesive wear, surface fatigue, and tribo-chemical reactions [24].

Erosion includes all types of wear, where damage is caused by impacting particles and/or a fluid (liquid, gas) [26]. The fluid can be single-phased (liquid or gas) or multi-phased (liquid/gas plus abrasive particles) [24].

Therefore, erosion can be assigned to the type of impact wear and abrasive wear, where a single or a combination of wear mechanisms takes place [27–29]. Depending on the composition of the tribological system, different types of erosion can be identified [23, 30]. **Liquid Impingement Erosion** occurs when liquid drops or jets continuously strike a material's surface. When vapor bubbles are formed in a flowing liquid due to “vacuum” zones and carried to regions with higher pressure and therefore implode, **Cavitation Erosion** occurs. Through the collapsing of the vapor bubbles, shockwaves have created that strike the surface with high speed, leading to elastic/plastic deformation and thus damage [31]. A gas stream causes **(Hot) Gas Erosion**. Not only solid particles are removed from the surface of the material but also ions and molecules through diffusion processes [26]. The primary erosion type which is dealt with in this work is **Solid Particle Erosion (SPE)**. The following paragraphs will give a short introduction to the topic.

Solid Particle Erosion occurs when a surface is hit by hard particles that are entrained by a fluid with high speed [29]. Besides the particle properties and fluid flow conditions, the mechanical properties of a material are the primary influence factors [32].

Two major types of material behavior regarding SPE are described - ductile and brittle failure [33–35]. **Figure 2** shows the correlation between impact angle and amount of erosion depending on the material behavior.

Ductile behavior is described by material removal due to severe plastic deformation at the site of impact. Eroding particles remove material due to cutting or plowing. In this case, the particles' low impact angles (20° - 40°) are causing the most considerable damage [33, 35]. This behavior is explained by ductile materials' generally low hardness and a high plastic deformation capacity [36].

Brittle behavior occurs in micro-cracks at the impact site, which propagate until failure. Brittle materials generally exhibit high hardness and, low plastic deformation capacity, leading to crack formation after reaching the stress limit [36]. At an impact angle of about 90° maximum, particle kinetic energy acts on the surface, and a significant material loss is caused at that angle [2, 33, 35].

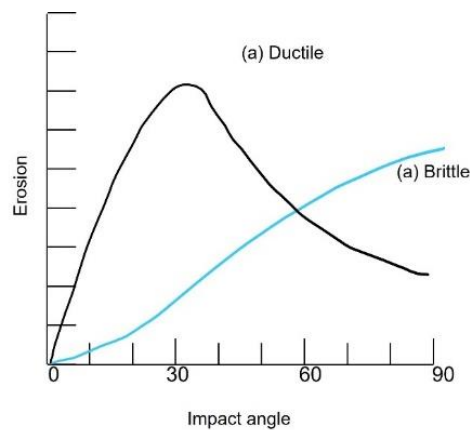


Figure 2: Correlation between impact angle and amount of erosion for a) Ductile behavior and b) Brittle behavior. Adapted from [2]

Apart from hardness (**H**), which is the material's ability to resist deformation under a given indentation, the Young's modulus (**E**), which is described as the elastic response of a material, and the fracture toughness (**K_C**), defined as the materials' ability to resist crack growth, are crucial [2]. Further possibilities to categorize materials are the **H/E** ratio [37], which indicates surface resistance to sliding wear, the **H³/E²** relationship, which measures the material's resistance to the onset of plastic deformation, and **H/K_C**, the index of brittleness [2].

In this diploma thesis, we investigate the influence of Mo on the structure and fracture-mechanical properties of TiB_{2+z} thin films. Such Ti_{1-x}Mo_xB_{2+z} coatings might be a promising candidate for new ternary diboride systems. Using 6-inch powder metallurgically produced targets obtaining a Mo content from $x = 0$ up to $x = 0.2$, thin films will be deposited using unbalanced DC magnetron sputtering on a lab-scale PVD system. The deposition is followed

by characterization of the coatings regarding structure, morphology, mechanical properties, and particle erosion resistance. For this purpose, analysis via scanning electron microscopy (SEM), nanoindentation and x-ray diffraction (XRD), and in-situ micromechanical testing will be conducted. This thesis aims to study the possibility of forming of a $Ti_{1-x}Mo_xB_{2+z}$ structure/solid solution. The focus lies on the effect of Mo on the mechanical properties such as hardness, Young's modulus, fracture toughness, and an application-oriented property that relates to the previous ones, the erosion resistance.

2. Physical Vapor Deposition (PVD)

Physical Vapor Deposition (PVD) describes a set of techniques for modifying surfaces by applying coatings to improve the function and durability of the coated material.

The underlying principle behind PVD is the evaporation of material from a solid or liquid target in a vacuum, followed by the transport of the vaporized material through a vacuum or plasma and condensation to the substrate [6]. This leads to the formation of a thin film on the substrate.

PVD processes are categorized as follows: vacuum deposition (evaporation), sputter deposition, and ion plating, as well as the reactive variants of the methods mentioned [6, 38].

Using PVD, various coatings can be deposited, as there are many possible target materials made of single elements or alloys. By using reactive gases, such as nitrogen, it is possible to form compounds through the reaction of the gas with the target material and thus the deposition of compound thin films. The average film thickness produced with PVD ranges from a few nanometers to several micrometers. The structures of PVD coatings are variable as it is possible to deposit monolayer, multilayer, or gradient compositions [6].

Some significant advantages of PVD are the diversity of possible coating materials (e.g., metals, alloys, carbides, nitrides, borides) and various usable substrate materials and sizes [39].

PVD processes are mainly used for optical, magnetic, and microelectronic parts and for the protection against tribological stress, oxidation, and corrosion [39].

2.1 DC Sputtering

Sputtering is the ejection of target atoms by bombardment with energetic ions coming from an ion gun, or a plasma accelerated in an electric field [6]. Surface atoms of the target are emitted due to momentum transfer from the bombarding ion [6, 38, 39]. The sputtered atoms are transferred into the gas phase and subsequently condensed on a substrate.

Different sputter configurations and conditions are used in practice, and these include Direct Current sputtering (DC sputtering), Magnetron sputtering, Radio Frequency (RF sputtering), and ion beam sputtering as well as the reactive versions of these [4, 38].

DC Sputtering requires two planar electrodes, the cathode, and the second one is the anode. The coating material (target) is mounted in front of the cathode (negative electrode) where a

potential is applied. A grounded potential and/or a bias is applied on the anode (positive electrode), where the substrates are placed. Additionally, the substrates can be heated or cooled depending on the process requirements [4, 6, 38].

For sputtering, the process chamber must be evacuated until a pressure from 10^{-5} to 10^{-6} mbar is reached. After evacuation, an inert process gas, in most cases argon (Ar), is continuously introduced into the chamber.

A glow discharge is obtained between the two electrodes by applying a DC potential (voltage), and by ionization of the process gas, plasma is built up. Plasma is defined as a weakly ionized gas containing ions, electrons, and neutrals in nearly equal amounts.

For a stable plasma the gas discharge must take place in the region of the abnormal glow discharge, where the whole cathode is covered by a glow, and the plasma fills the region between the two electrodes. Characteristically, an increase in power leads to a simultaneous increase in voltage and nearly uniform current density levels at the cathode [5]. Between anode and cathode various dark and luminous regions alternate. Closest to the cathode, the cathode glow region is found and next in line is the cathode dark space. Between the cathode dark space and the following negative glow, a drop in discharge voltage (cathode sheath) occurs, resulting in the appearance of an electric field [5]. Last in line is the anode. As the cathode (target) is negatively biased, the Ar^+ ions are accelerated towards the target through the electric field, and upon impact (momentum transfer), mainly neutral atoms are sputtered out of the target [4, 38]. Simultaneously to the sputtering of metal atoms from the cathode, secondary electrons are created for further ionization of the Ar-gas [5, 6]. The sputtered atoms are transported towards the substrate (anode) and condensation followed by film nucleation and growth occurs.

The deposition rates of DC sputtering are lower than other techniques due to the low efficiency of using electrons to create ions; additionally, high voltages are required. Hence, magnetron sputtering systems are preferred [4, 38].

2.2 Direct Current Magnetron Sputtering (DCMS)

For magnetron sputtering, strong permanent magnets are circularly attached behind the target leading to a magnetic field parallel to the cathode in addition to the electric field between the two electrodes [38]. The Lorentz force forces electrons and secondary electrons to move along the magnetic field lines in a closed loop [38]. Consequently, electrons are trapped along the magnetic field, giving a higher collision rate between gas molecules and electrons [38]; hence an efficiency an efficiency increase in the ionization of the process gas is observed [4]. The magnetic field is also responsible for a higher plasma density at the cathode, and the loss of electrons due to recombination at the chamber walls is eliminated. Magnetron sputtering, therefore, achieves high deposition rates [4]. In **Figure 3**, the general principle of magnetron sputtering is displayed.

Consequently, targets used in magnetron sputtering typically show a so-called “race-track”, where most atoms have been sputtered out along the magnetic field [4].

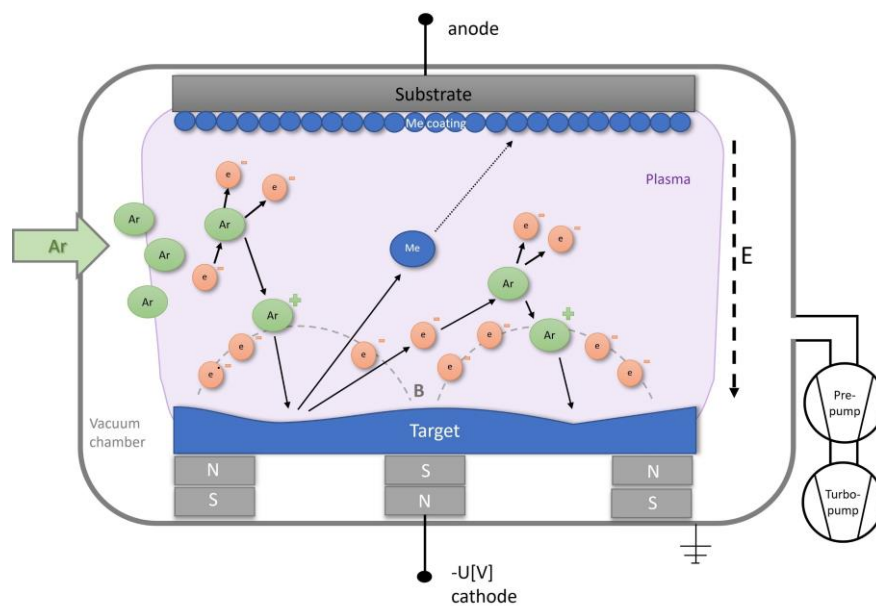


Figure 3: DC magnetron sputter configuration and principle of target sputtering of a PVD system. Figure was adapted from [40]

2.3 Thin film growth

Films grow through the continuous nucleation and condensation of arriving atoms. The formation of thin films undergoes different stages of nucleation and growth onto the surface of the substrate. These stages include adsorption/condensation and desorption, surface diffusion, chemical binding, and (nuclei growth, interface formation) [6, 41].

The film material, the flux (J), the kinetic energy (E), the growth temperature T_s , the substrate material, and the flux of contaminants are the factors that determine nucleation and growth kinetics, microstructural evolution, and properties of the coating/thin film. Therefore the deposition parameters such as temperature, pressure, and bias potential play a central role in the growth of thin films [1, 6]. Nucleation and growth depend on the interaction between film and substrate atoms. Film formation is a heterogeneous nucleation process, which means adatoms condense at the substrate, leading to nuclei formation and their growth once supersaturation is reached. Depending on the surface energies – surface energy is described by the Young's equation (**Equation (1)**)– three growth modes can occur. A schematical drawing is shown in **Figure 4** [1, 5, 41].

$$\gamma_B = \gamma^* + \gamma_A \cos\varphi \quad \text{Eq.(1)}$$

With:

- γ_B surface energy of the substrate
- γ^* interface energy (film-substrate)
- γ_A substrate energy of the film
- φ wetting angle

(a) Volmer-Weber (Island)

Through nucleation of small stable clusters on the surface and growth in three dimensions, so-called islands are formed. This occurs due to the stronger bond of the atoms (and/or molecules) to each other than to the surface of the substrate. Island growth occurs at $\varphi > 0$ and when $\gamma_B < \gamma_A + \gamma^*$ is fulfilled.

(b) Frank-Van der Merwe (Layer-by-layer)

Planar sheets are created when the smallest stable nucleus extends in two dimensions. In this case, the film atoms are more strongly bound to the substrate than each other. After the first monolayer is completed, it is covered by a second one.

Contrary to Island growth, Layer-by-Layer growth occurs when occurs $\phi < 0$ and $\gamma_B > \gamma_A + \gamma^*$ are fulfilled.

(c) Stranski-Krastanov (Layer plus Island)

With film thickness, the interface energy is increased, and Layer-plus-Island growth can occur. In this case, a combination of island and layer growth is present. At first, one (or more monolayers) are formed until island growth becomes energetically more favorable.

The film growth and nucleation modes determine surface morphology, grain size, film density, and surface area.

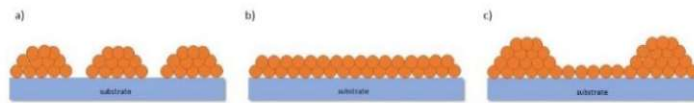


Figure 4: Schematic of the three modes of thin film growth: a) Volmer-Weber (Island), b) Frank-Van der Merwe (Layer-by-layer), and c) Stranski-Krastanov (Layer plus Island). Adapted from [4].

To better understand how the microstructure of thin films and the deposition parameters are interconnected, Movchan and Demchishin presented the first Structure Zone Model (SZM) for thick films obtained by evaporation in 1969. The homologous temperature T_h , defined as the film growth temperature T divided by the melting temperature of the film material T_m , is related to the development of different microstructures. According to Movchan and Demchishin, three zones can be distinguished depending on T/T_m .

Characteristically, zone I with $T/T_m < 0.25/0.3$, is a fine-grained (textured and fibrous with domed tops) [4, 42], highly porous structure due to low surface diffusion (low adatom mobility)

at low temperatures. In zone II with $0.25/0.3 < T/T_m < 0.5$, uniform columnar grains are formed due to the onset of surface diffusion. The grains are separated by distant, dense, intercrystalline boundaries [4].

With its even higher temperatures, $T/T_m > 0.5$, zone III is characterized by bulk diffusion and recrystallization, which results in a dense, coarse-grained structure [42].

As magnetron sputtering became more relevant further research by Thornton (1975/77) extended the model by adding the process pressure. Between zone I and zone II, a transition zone (zone T) was introduced, consisting of dense fibrous grains without voids between the grains [4, 42, 43]. The pressure influences the microstructure as the number of collisions of sputtered atoms with the process gas increases with increasing pressure [42]. That means a lower pressure leads to a higher film density [4, 43]. The SZM developed by Thornton is shown in **Figure 5**.

Further modifications of the SZM were made by Messier et. al. (1984), who added the dependence on the energy of the incident particles. They stated that the transition zone T becomes more stable with increasing particle energy [4, 42, 44].

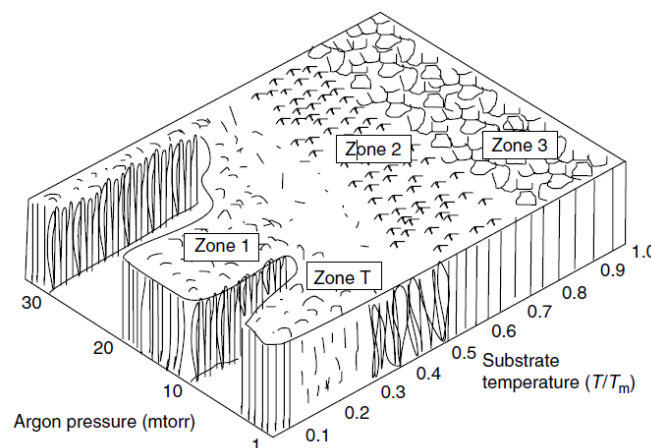


Figure 5: SZM by Thornton. Taken from [4]

The latest version of the SZM was presented by Anders in 2010 [42]. Also, the effects of ions on the film growth are taken into consideration. To achieve a universal applicable Structure-Zone-Diagram, the axes were generalized, so the following axes were obtained:

- (a) The generalized Temperature T^* which includes the homologous temperature T_h as well as a temperature shift caused by the potential energy of particles arriving on the substrate.
- (b) The normalized energy E^* describes effects caused by the kinetic energy of bombarding particles, such as displacement and heating effects
- (c) The net film thickness t^* also includes thickness reduction through densification and ion etching.

The structure zone diagram presented by Anders is shown in **Figure 6** [42].

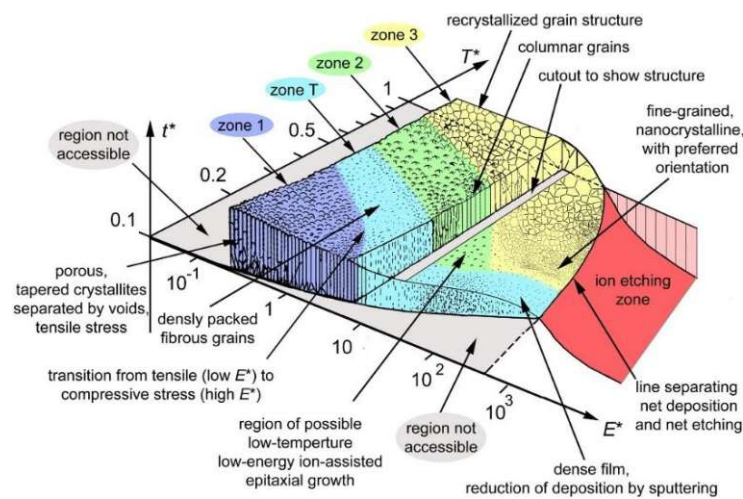


Figure 6: Structure zone diagram by Anders [42]

3. Transition Metal Diborides

Transition Metal Diborides (TMB₂) consist of boron and a transition metal (TM). Boron is the 5. element in the periodic table. It obtains three valence electrons and is the lightest non-metal with a tendency to form covalent B-B bonds [45, 46].

Transition metals are chemical elements in groups III to XII that are, according to IUPAC, defined as “an element whose atom has an incomplete d sub-shell, or which can give rise to cations with an incomplete d sub-shell” [47]. The general properties of those metals are high hardness and tensile strength, high melting and boiling points, and good electrical and thermal conductivity [48]. For PVD coatings, TM of groups IV to VI are attractive; these are Ti, V, Cr, Zr, Nb, Mo, Hf, Ta, and W. **Figure 7** shows melting temperatures and the preferred crystal structure of these transition metal diborides.

	Group IV 4 valence e ⁻	Group V 5 valence e ⁻	Group VI 6 valence e ⁻
Period IV	TiB ₂	VB ₂	CrB ₂
	α-AlB ₂ 3203 °C 0.94	α-AlB ₂ 2750 °C 0.99	α-WB ₂ 2200 °C 0.99
	ZrB ₂	NbB ₂	MoB ₂
Period V	α-AlB ₂ 3245 °C 0.89	α-AlB ₂ 3036 °C 0.96	ω-WB ₂ 2140 °C 0.21
	HfB ₂	TaB ₂	WB ₂
Period VI	α-AlB ₂ 3377 °C 0.97	α-AlB ₂ 3140 °C 0.93	ω-WB ₂ 2362 °C 0.21

Figure 7: Overview of group IV to VI TMB₂ with corresponding melting points and preferred structure.

Diborides have gained quite some interest in the research of thin films. Due to the favorable properties of their corresponding bulk materials, e.g., a high hardness, high melting point, elastic modulus chemical stability, and high electrical conductivity, they are promising for future applications as wear and corrosion-resistant coatings and decorative coatings. These preferable properties are attributed to the covalent bond character of borides [9]. On the other hand, a significant drawback of transition metal diborides is their limited oxidation resistance. [8, 20, 30]

Usually, TMB_2 prefer to crystallize in the α - AlB_2 structure (space group 191, hexagonal $P6/mmm$) or the ω - W_2B_5 structure (space group 194, hexagonal $P6_3/mmc$). They are built up from close-packed TM layers with boron occupying the interstitials [20]. In the case of the AlB_2 structure, graphite-like honey-combed atomic sheets of B alternate with hexagonal-closed packed TM layers, the structure is shown in **Figure 8** [14, 20]. The ω - W_2B_5 structure is formed from metal layers with alternating flat and puckered boron hexagons the metal layers [14].

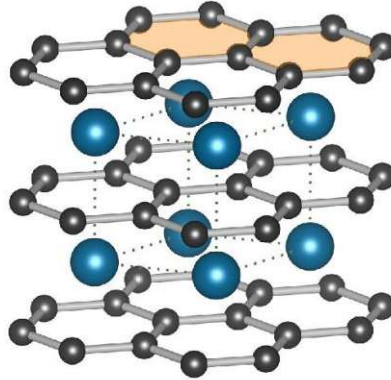


Figure 8: Schematics of the α - AlB_2 structure (space group 191, hexagonal $P6/mmm$). The black spheres symbolize B and the blue spheres the M atoms.

TiB_2 and MoB_2 , the subject of this work, will be further explained in the following sections.

3.1 Ti - B System

Within the Ti-B system's binary phase diagram (**Figure 9**), titanium diboride only exists in a narrow homogeneity range between 65.6 and 66.7 at% boron with a high melting point of 3225 °C [12]. TiB₂ crystallizes in the hexagonal α -AlB₂ structure, where boron is located as a covalently bonded network between the closed-packed Ti-planes. [12, 49, 50]. Other boride phases that are present in this system are TiB and Ti₃B₄.

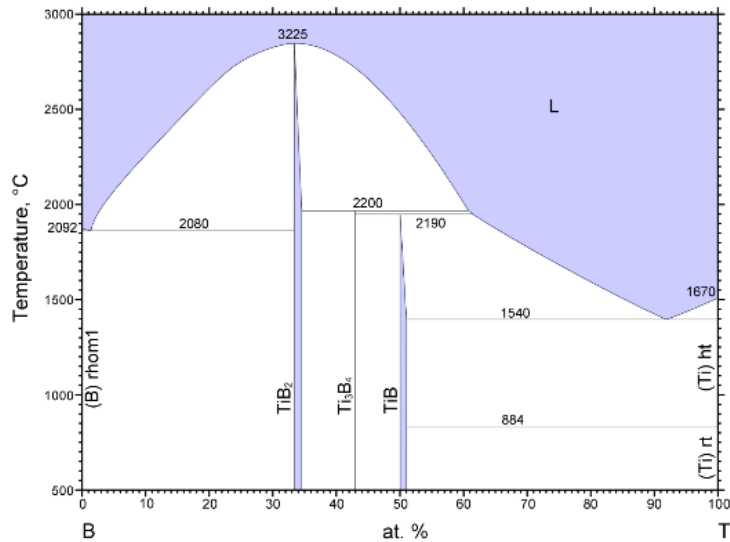


Figure 9: Binary Ti-B phase diagram. Taken from [51]

TiB₂ is a ceramic material with a density of 4.52 g/cm³, high melting point, thermal stability, and brittle character. Hardness values range from 20 GPa up to > 40 GPa, strongly depending on the used deposition technique, parameters, composition, and characterization method, as reported in the literature [12, 50, 52].

Sputtered TiB₂ often exhibits an excess in boron content, which leads to the formation of a so-called tissue phase at the grain boundaries [12, 52].

The stoichiometry is strongly dependent on the deposition parameters pressure, target-substrate distance, and angle. It was shown that B tends to be sputtered more along the target normal, whereas Ti shows a much broader distribution. An explanation for this phenomenon is the difference in mass between Ti and B. The Ti/B ratio correlates to the pressure and target-substrate distance. [52, 53]

Using certain deposition parameters, TiB_2 preferentially grows in a 0001 – orientation, being a reason for the high hardness, whereas for (10 $\bar{1}$ 1) and (1000) oriented coatings, a decreasing hardness was observed [52]. This assertive anisotropic behavior of hexagonal diborides was theoretically confirmed for ZrB_2 and TiB_2 and experimentally for WB_{2-z} based thin films [54–56].

Regarding the fracture toughness of sputtered TiB_2 , limited data is available. However, values for different stoichiometry have shown to depend on the tissue phase proportion, and range from 2.51 to 3.02 $\text{MPa}\sqrt{\text{m}}$ [52].

3.2 Mo - B System

Present bulk phases in the binary Mo-B phase diagram, shown in **Figure 10**, are, on the one hand, pure Mo and βB and, on the other hand, several boride phases. Starting on the boron-rich side and moving to the molybdenum-rich side, the $\text{Mo}_{0.8}\text{B}_3$, MoB_2rt , and MoB_2ht , the $\alpha\text{-MoB}$ (rt) and $\beta\text{-MoB}$ (ht), $\text{Mo}_3\text{B}_2\text{ht}$, and finally, Mo_2B are present [57, 58].

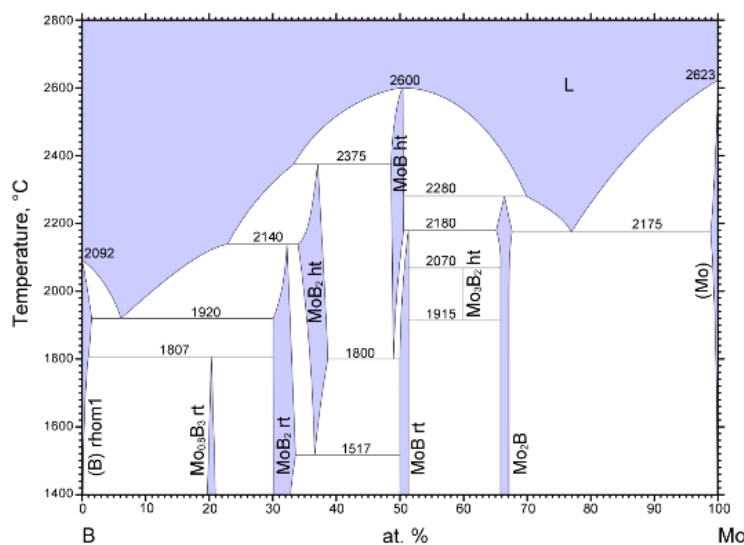


Figure 10: Binary Mo-B phase diagram. Taken from [57].

Regarding TM_2B_2 coatings, the MoB_2ht phase, which crystallizes in the hexagonal AlB_2 -type and is only stable at temperatures >1500 °C, is interesting. At room temperature, the MoB_2 with the rhombohedral crystal structure (hR18) is stable [57, 58]. In literature, the stability and formation of molybdenum boride phases is still a topic without a conclusion [15, 58, 59]

Data on DC magnetron sputtered MoB₂ is very little. Coatings with a nanocomposite structure and hardness of about 29 GPa were first reported [15]. Also, the presence of a boron-rich tissue phase was observed. [15, 58] α-MoB₂ can be considered ductile after Frantsevich and Pugh while only slightly brittle after Pettifor [14].

3.3 Ternary System Ti-Mo-B – Mo alloying

So far, the knowledge on ternary transition metal diborides is limited. However, these systems seem promising candidates as protective thin films for further improvement of mechanical properties, oxidation, and corrosion resistance. Examples of systems that have been already investigated are $W_{1-x}Ta_xB_{2-z}$ [16], $W_{1-x}Al_xB_{2-z}$ [17], and $W_{1-x}V_xB_{2-z}$ [10].

In the present work, the ternary diboride $Ti_{1-x}Mo_xB_2$ is suggested/proposed to combine TiB_2 , which is hard and brittle, and MoB_2 , a ductile material. This assumption is checked in the first step by Density Functional Theory (DFT) calculations using Vienna Ab-Initio Simulation Package (VASP).

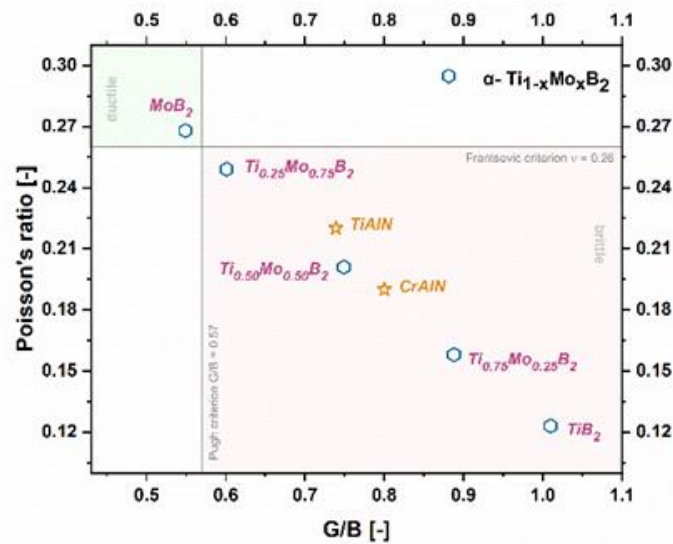


Figure 11: Poisson's ratio over the G/B ratio for the two binary systems TiB_2 and MoB_2 , as well as different ternary compositions of the $Ti_{1-x}Mo_xB_{2±z}$ system.

Screening the alloying of TiB_2 with Mo using elastic constants (bulk modulus B, shear modulus G, and Poisson's ν) and categorizing the results after Pugh and Frantsevich supports the previously made assumption. **Figure 12** shows that compositions alloyed with Mo are shifted to smaller G/B ratios and higher values of Poisson's ratio.

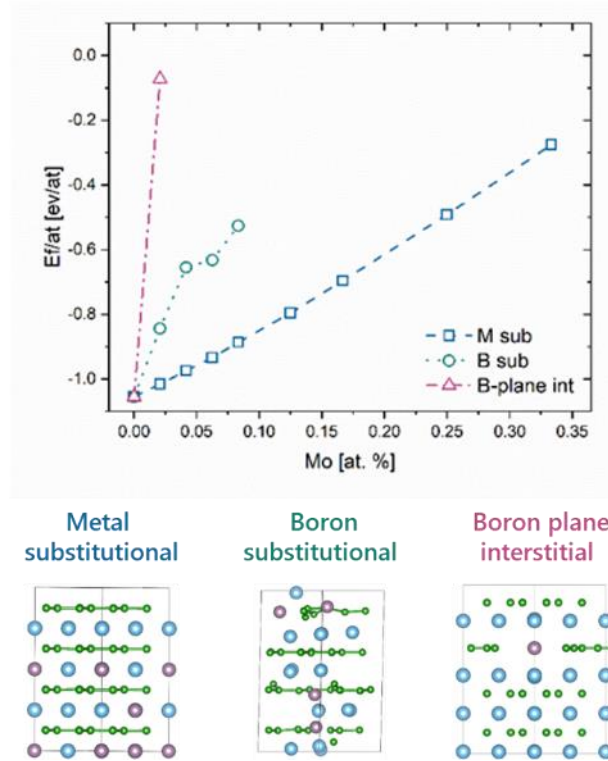


Figure 12: Results of DFT calculations for the energy of formation E_f for different scenarios of Mo incorporation into the crystal lattice: Metal substitutional, Boron substitutional, and Boron plane interstitial. B atoms are shown in green, Mo in violet and Ti in blue.

To determine the most probable place Mo occupies in the crystal lattice, the energy of formation (E_f) for different scenarios has been calculated using Density Functional Theory (DFT). For two base systems, TiB_2 and MoB_2 , the values for E_f are -1.01 eV/atom and -0.28 eV/atom, respectively. A supercell ($2 \times 2 \times 2$) with 48 Atoms (16 Me and 32 B) was taken, and E_f for Mo substitutional for Ti and B, respectively, and Mo as interstitial on the B plane was calculated, starting from TiB_2 (0 at% Mo) up to MoB_2 (33 at% Mo). According to those results (shown in **Figure 12**), Mo as metal substitutional obtains the lowest E_f , which means it is the most probable way of incorporating Mo.

Based on this theoretical work, the ternary diboride system $Ti_{1-x}Mo_xB_2$ is a promising candidate as a hard and ductile protective thin film. The calculations themselves were not part of the present work but are listed here for the sake of completeness and understanding.

In a second step, $Ti_{1-x}Mo_xB_2$ coatings with different contents of Mo are deposited using PVD and characterized regarding their structure, composition, and mechanical properties. The following sections deal with the coating synthesis and the used characterization techniques.

4. Coating Synthesis

The TiB₂ and TiMoB₂ coatings were deposited using DC magnetron sputtering. In-house manufactured lab-scale deposition system NOREIA, equipped with two 6-inch and two 3-inch cathodes in an angular alignment, was used. The incident angle between substrate normal and target of the two confocally arranged 6-inch targets is about 20° [60].

For the depositions, 6-inch powder-metallurgically manufactured targets with a molybdenum backplate (Plansee Composite Materials GmbH) of the following compositions were used:

TiB₂/C 99/1 mol%, TiB₂/MoB 95/5 mol%, TiB₂/MoB 90/10 mol%, TiB₂/MoB 80/20 mol%

Depositions were done using one target and for variation of the composition co-sputtering of two different targets.

As substrate materials, silicon platelets (100)-oriented 20x7x0.38 mm, sapphire (1-102)-oriented 10x10x0.53 mm³, polished austenite 20x7x0.8 mm³, QRS, Ti-Al6-V4 25x25 mm and polycrystalline Al₂O₃ (polished & unpolished) 20x7x0.38 mm were used. Before mounting, the substrates were ultrasonically cleaned in acetone and ethanol for five minutes each.

Before the actual coating, plasma etching was conducted as an additional cleaning step for the substrates. Therefore, a voltage of -500 V, 65 sccm Ar, and a working pressure of 60 μbar were applied for 15 min.

A process gas flow (Ar-flow) of **30 sccm** and a working pressure of **4 μbar** were applied for all coatings. The current at the target was set to **4.2 A**, and a bias voltage of **-50 V** was utilized. The heater temperature was set to **700 °C**, which corresponds to a substrate temperature of **450 °C**, and a z-distance (target-substrate distance) of **150 mm** was chosen.

The received coatings were analyzed regarding their composition, structure, and mechanical properties. Used instrumentation/experiments is/are explained in the following section.

5. Characterization Techniques

Many techniques have been used to characterize the deposited coatings concerning crystal structure and mechanical properties like hardness and fracture toughness. The description of these methods is to be found in the following subchapters.

5.1 Scanning Electron Microscopy (SEM)

Scanning electron microscopy (SEM) is a popular technique for enlarging features otherwise invisible to human sight [61]. Compared to a standard light microscope, the resolution is much higher, and therefore much higher magnifications are possible. The main principle of SEM is based on the acceleration of an electron beam onto the surface of a sample in a vacuum and image acquisition by a detector while scanning the sample's surface. The SEM instrument consists of the electron column and the chamber, kept under vacuum, and the microscope control (computer). The gun generates the electron beam, accelerated by a voltage up to 50 kV, and modified to reduce the beam diameter through (electro)magnetic lenses. The focused beam is then scanned over the surface of the sample in a raster [61, 62].

Various information can be gathered through different interactions between the primary electrons (beam) and the sample. Secondary electrons (SE) created by inelastic scattering are used to investigate the morphology of a sample. Backscattered electrons (BSE), created by elastic scattering, are used for chemical/element information of the material, as its contrast is dependent on the atomic number. Other interactions are characteristic X-rays, used for the qualitative and quantitative chemical analysis via EDS (energy dispersive x-ray spectroscopy) [61]. Scanning electron microscopy is used as a standard technique for cross-sections/determining the film thickness of coatings.

In this work, SEM is mainly used to acquire cross-sectional images to get a closer look at the microstructure of the deposited thin film. Furthermore, in-situ cantilever bending tests were carried out using a FemtoTool FT-NMT04 nanoindentation system within the SEM chamber. All experiments were conducted on an FEI Quanta 200 system and Zeiss Sigma 500 VP system with field emission guns.

5.2 Transmission Electron Microscopy

For a more detailed structural analysis of the thin films, transmission electron microscopy (TEM) is the technique of choice. TEM provides information about crystal structure, crystal phases, and composition of a material. Features within the crystal structure, such as grain boundaries or dislocations, can be made visible by this method. TEM samples must be very thin in a range of some tens of nm thickness so that the electron beam can pass through the sample.

Image acquisition starts with the generation of an electron beam in an electron gun, which is then focused by electromagnetic lenses. The sample is placed in the beam path, and the beam passes through the specimen, causing interactions between the two. The sample scatters parts of the electrons, and other parts are transmitted through the samples. The density and thickness of the sample are crucial for the number of transmitted electrons. Under the sample, the transmitted portion is focused on a fluorescent screen/CCD camera, and an image is produced [63]. Transmitted electrons that have not been diffracted are used for bright-field imaging, whereas diffracted electrons are used for dark-field imaging [64].

With the corresponding tools and detectors, various analytical information can be obtained via a transmission electron microscope.

Scanning Transmission Electron Microscopy (STEM) offers an interconnection between SEM and TEM. The electron beam of the TEM is scanned over the sample, and image acquisition is quite similar to SEM, except for different detection techniques [64].

Selected Area Electron Diffraction (SAED) is used to determine the crystal structure of a material by the pattern created due to the diffraction of the electron beam by the sample.

An FEI TECNAI F20 transmission electron microscope is used in the present work. Bright-field and dark-field images were taken. Additionally, SAED analysis was performed.

5.3 Nanoindentation

To determine the mechanical properties, hardness (H) and Young's modulus (E) of thin films, nanoindentation is used. Standard hardness measurement techniques such as Vickers or Brinell tests are not suitable for thin films due to the thickness in the μm range. One significant advantage of nanoindentation is that it is possible to measure only the coating properties without influences of the substrate without removing the coating from the substrate. To ensure only the coating is measured, the Bückle-rule applies, which states that the indentation depth should be smaller than 1/10 of the coating thickness. Additionally, the elastic modulus of the coating can be determined directly, which is not possible with other methods. For the measurement, a diamond tip (mostly Berkovich geometry) is pressed into the material up to a maximum load P_{max} followed by unloading. Load and indenter position (indentation depth) are continuously recorded during the measurement. A typical load-displacement curve is shown in **Figure 13**.

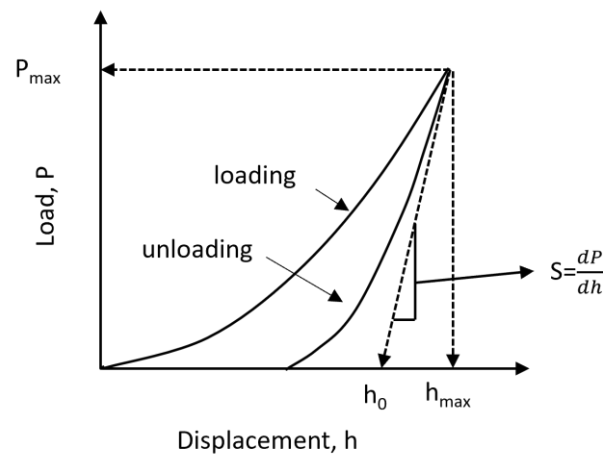


Figure 13: Typical load-displacement curve derived from nanoindentation. With P_{max} (peak load), h_{max} (max. displacement) and S (initial unloading contact stiffness) being the most important values. Adapted from [65]

From the recorded load-displacement curves hardness and elastic modulus are determined following the Oliver-Pharr Method [65]. An “area function” is used to correct the data to exclude influences of the changing tip geometry. The area function is obtained by calibration, using a standard material (fused silica) to determine the deviation of the actual indenter tip from the ideal indenter tip geometry.

The hardness is calculated according to equation (2) with:

$$H_{indent} = \frac{P_{max}}{A_c} \quad \text{Eq.(2)}$$

H_{indent} is the indentation hardness in GPa,

P_{max} the maximum force in mN

A_c the projected contact area of hardness impression in μm^2

The Young's modulus is calculated according to equation (3):

$$\frac{1}{E_r} = \left(\frac{1 - \nu^2}{E}\right)_{Ind} + \left(\frac{1 - \nu^2}{E}\right)_{Mat} \quad \text{Eq.(3)}$$

With:

ν the Poisson's ratio

E_r the reduced Young's modulus

E the elastic modulus in GPa

A more detailed description of the calculations is given in [65] and [66].

A CSIRO UMIS Nanoindentation system with a diamond Berkovich tip was used in the present work. At least 25 indents with forces ranging up to 40 mN were conducted. For the calculation the following tip characteristics apply: $E = 1050$ GPa and Poisson's ratio $\nu = 0.07$. Calibration of the system was conducted with a fused silica sample ($E = 72.5$ GPa, $H = 10$ GPa). All hardness measurements were performed on austenite substrates.

5.4 X-ray Diffraction Analysis (XRD)

X-ray diffraction (XRD) is a commonly used method for structural analysis of crystalline materials. Crystallographic data such as lattice parameters, crystal structure, size and orientation, and stresses can be determined. In general electromagnetic radiation with wavelengths between 1 nm and 1 pm is called x-ray radiation [67].

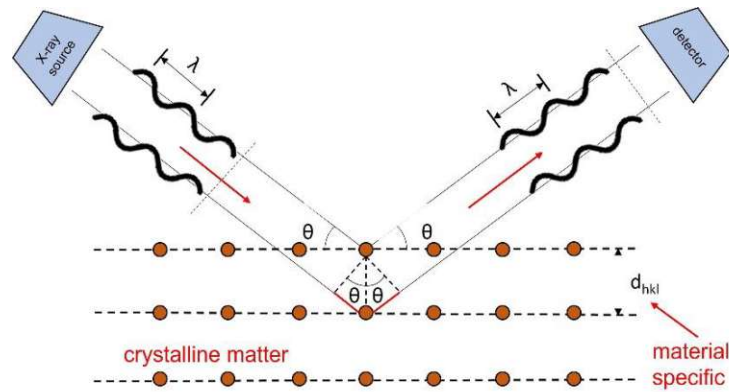


Figure 14: Schematic of X-ray diffraction on a crystal plane (Bragg's Law). Adapted from [68]

The principle of XRD analysis is based on the diffraction of X-rays on periodic structures like crystals. When X-rays interact with matter, elastic scattering occurs, which means the incident wave and secondary wave frequency are equal [68]. Upon impact of the incident X-rays with the electrons of a crystal, which acts as a grating, diffraction occurs, and this interaction between the X-rays and the crystalline material leads to constructive interference if the conditions of Bragg's Law (**Equation (4)**) are fulfilled. This means that the angle of incidence and the angle of scattering must be equal, and the spacing of the crystal lattice planes must correspond to the length scale of the wavelength of the x-rays, as schematically drawn in **Figure 14**. Occurring diffraction peaks are characteristic of the distinct crystal substance, and by comparison with a database, the crystal structure can be identified.

$$n\lambda = 2d \sin(\theta) \quad \text{Eq.(4)}$$

With:

λ the wavelength

d the distance between adjacent crystal lattice planes

θ the Bragg angle

n the order of reflection

For the experiments in the present work, a Philips XPERT diffractometer with a Cu-K α ($\lambda=1.54 \text{ \AA}$) source in the Bragg-Brentano configuration was used. The measurements were conducted at Bragg angles ($\theta = 15$ to 130°).

5.5 Micromechanical Testing

Before addressing the determination of the fracture toughness through micromechanical testing some fundamentals of fracture mechanics are given. Fracture toughness is understood as the resistance of a material against crack propagation. The material characteristic attributed to fracture toughness is the critical stress intensity factor K_{IC} .

Fracture mechanics deals with the cracks and the load needed to cause crack propagation, consequently leading to the failure of a component. Cracks are considered sharp notches. By the position of the stress field in relation to the crack, the distinction between three characteristic loading cases (mode I to III) is made. **Mode I** is present when the crack proceeds perpendicularly to the occurring normal stress. This is the case for tensile and compressive (bending) loading. **Mode II** describes all shear stresses that cause opposite sliding of the crack surfaces in the crack direction. **Mode III** is present when the crack surfaces slide transverse to the crack. This is the case for non-planar shear stress conditions. [69, 70]

Based on linear elastic fracture mechanics theory, the fracture toughness can be determined/calculated. In general, this theory is only valid for ceramics with little to no plastic deformation but can be applied for metals if the plastic deformation zone is smaller than the so-called K-dominated stress field. The stress field gets a singularity when the stress at the crack tip becomes infinite. The stress intensity factor K describes this stress state; for mode I, it is denoted as K_I [69–71]. When the stress intensity factor reaches a critical value, K_{IC} crack propagation occurs [71].

K_{IC} is defined as shown in **equation (5)** [69]:

$$K_{IC} = \sigma_c \sqrt{\pi a} Y \quad \text{Eq.(5)}$$

With:

σ_c the critical stress

a the crack length

Y the geometry factor

The method of in-situ micromechanical cantilever bending tests was chosen to determine the fracture toughness. An image of such micro-cantilever and important geometrical information is shown in **Figure 15**. This technique for investigation of the fracture toughness of coatings without substrate influence using a pre-cracked micro-beam was proposed by [72].

This method's reproducibility and measurement accuracy was assessed by [73]. Also, in the equation used for evaluation (**equation (6)**) the fracture toughness was given by [73]. Their work related the geometry factor Y (equation (4)) to the cantilever geometry by Finite element method (FEM) calculations. The a/w -ratio should lie between 0.05 and 0.45, and the aspect ratio of the beam dimensions should be approximately $H:L:w:B = 2:5:2.1:1.7$ [73]. Due to Focused Ion Beam (FIB) milling, the cantilever geometries can vary to a certain extent, but it was shown that for rectangular cantilevers that slight variations in the geometry do not influence the resulting fracture toughness [71].

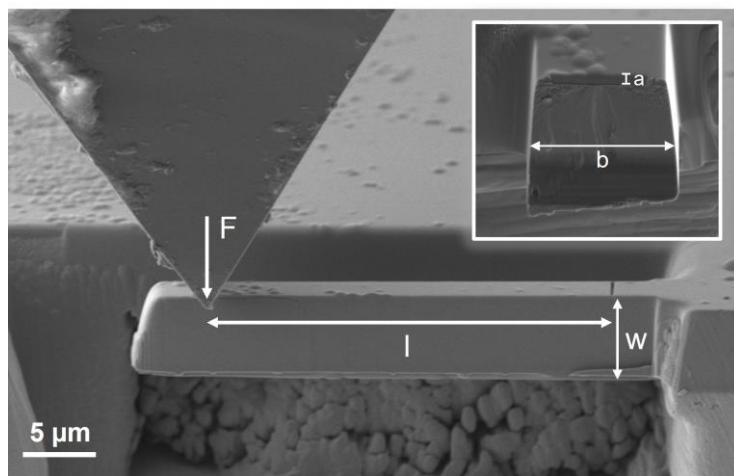


Figure 15 Image of a micro-cantilever and relevant geometrical information (l =length of the cantilever, w =film thickness, a =initial crack length and b =cantilever width)

To calculate the fracture toughness obtained by in-situ micromechanical tests, **equation (6)** is used [73]:

$$K_{Ic} = \frac{P_{max} l}{B w^{\frac{3}{2}}} \left(1.46 + 24.36 \left(\frac{a}{w} \right) - 47.21 \left(\frac{a}{w} \right)^2 + 75.18 \left(\frac{a}{w} \right)^3 \right) \quad \text{Eq.(6)}$$

With:

- P_{max} the maximum force
- l the length of the cantilever
- B the width of the cantilever
- w the film thickness
- a the initial crack length (notch)

Micro-cantilevers were manufactured by FIB milling. Therefore, a small piece of the coated substrate (austenite) is ground and polished, followed by cantilever preparation. In this case, pre-notched cantilevers are prepared. The bending experiments are conducted within an SEM chamber using an in-situ nanoindentation instrument. A diamond indenter tip is pressed into the cantilever until fracture while continuously recording the load-displacement data.

The FIB system used in this work for the preparation of the cantilever is ThermoFisher Scios 2. Bending tests are conducted in the already mentioned SEM systems with a FemtoTools NMT-04 in-situ nanoindentation system.

5.6 Solid Particle Erosion Test ASTM G76

Following ASTM G76, the resistance of the coatings against SPE is determined using an DUCOM Air Jet Erosion Tester (see **Figure 16**). Through a nozzle compressed air accelerates abrasive particles towards the sample surface. Different impingement angles, air pressure and particle velocities can be set [34, 74].

Before testing actual samples, the correct amount of eroding material (abrasive feed rate) must be checked, and an uncoated substrate is eroded as a reference/calibration. Then the actual coated samples are tested. The used parameters are listed in **Table 1**. The extent of erosion/material loss is determined by weighting the sample before and after the test and calculating the weight difference corresponding to the material loss. This is plotted against time.

Table 1 Particle Erosion Test parameters chosen according to ASTM G76

Test parameters	ASTM G76
Temperature	RT
Impingement Angle	30 °
Abrasive material	Al ₂ O ₃ (white corundum)
Distance Nozzle-Sample	15 mm
Particle Size	F240 (50 µm)
Estimated Particle Speed	70 m/s
Abrasive Feed Rate	2 g/min
Test Duration	60 sec increments



Figure 16 DUCOM Air Jet Erosion Tester

5.7 Further Techniques

The chemical composition of the deposited thin films was analyzed by liquid inductively coupled plasma optical emission spectroscopy LICP-OES. LICP-OES on an iCAP 6500 RAD Thermo Fisher Scientific system. The coating on sapphire substrates was dissolved in a mixture of 1 mL HNO₃ and 0.25 mL HF and heated for 15 min to a temperature of 60 °C until the coating and substrate were fully dissolved. Subsequently, the derived solution was diluted to a final volume of 20 mL with a mixture of 3% HNO₃ and 0.3 % HF. Quantification was done via external calibration using matrix-adjusted standards [75].

Annealing experiments of the thin films were conducted on polycrystalline Al₂O₃ substrates in a Centorr Vacuum Industries Series LF vacuum annealing furnace. Temperatures of 500 °C to 800 °C in 100 °C increments and annealing times of 1 h and 10 h were chosen for each temperature.

6. Results and Discussion

TiB_{2+z} and Ti_{1-x}Mo_xB_{2+z} thin films were deposited using DC magnetron sputtering. The first set of coatings was prepared and analyzed to overview the system. Three states out of these first depositions were chosen and redeposited for more detailed investigations. All coatings were characterized by the methods described in Chapter 4. In the following sections, the results of this thesis are presented and discussed.

6.1 Preliminary depositions

Using the parameter set described in **chapter 4**, thin films were deposited. For the variation of Mo content, different sets of targets (**Table 2**) were either sputtered alone or co-sputtered. A deposition time of 60 min was chosen for these coatings. All coatings were deposited on silicon (100)-oriented, sapphire (1-102)-oriented, and austenite substrates.

Table 2: Overview of deposited thin films, the used targets and their compositions, and the resulting contents of the individual elements within the thin films, determined by ICP-OES

Thin film	Target Composition	Thin film composition		
		Ti [at%]	Mo [at%]	B [at%]
TiB _{3.1}	TiB ₂ /C 99/1 wt%	24.64±0.31	-	75.36±0.31
Ti _{0.96} Mo _{0.04} B _{2.21}	TiB ₂ /C 99/1 wt% + TiB ₂ /MoB 95/5 mol%	29.80±0.09	1.27±0.01	68.92±0.08
Ti _{0.94} Mo _{0.06} B _{1.94}	TiB ₂ /MoB 95/5 mol%	31.87±0.44	2.17±0.02	65.95±0.42
Ti _{0.90} Mo _{0.10} B _{1.95}	TiB ₂ /MoB 95/5 mol% + TiB ₂ /MoB 90/10 mol%	30.92±0.20	3.00±0.02	66.08±0.23
Ti _{0.88} Mo _{0.12} B _{1.59}	TiB ₂ /MoB 90/10 mol%	34.21±0.05	4.46±0.01	61.33±0.04
Ti _{0.71} Mo _{0.29} B _{0.8}	TiB ₂ /MoB 80/20 mol%	43.21±0.50	12.39±0.12	44.40±0.62
Ti _{0.79} Mo _{0.21} B _{1.65}	TiB ₂ /MoB 90/10 mol% + TiB ₂ /MoB 80/20 mol%	31.08±0.23	6.72±0.12	62.20±0.35
Ti _{0.71} Mo _{0.29} B _{0.80}	TiB ₂ /MoB 80/20 mol%	43.21±0.50	12.39±0.12	44.40±0.62

The compositions (measured via ICP-OES) of the deposited coatings are shown in **Table 2**. Mo contents between zero for the pure TiB₂, and a maximum of 12.39 at% for the coating deposited with the highest Mo-containing target, are found. The change in Ti and B content is shown in **Figure 17a**). What is immediately noticeable, is that Ti increases and B decreases with increasing Mo content.

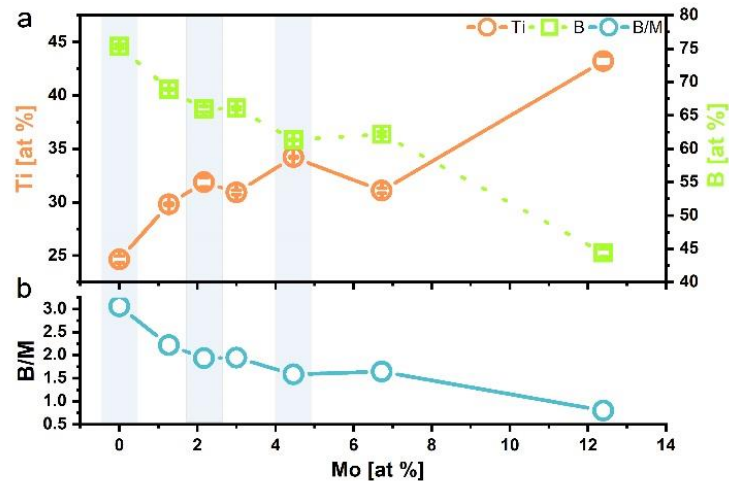


Figure 17: The progression of Ti and B over the Mo content within the deposited coatings a). The influence of Mo on the boron to metal (B/M) ratio is shown in b).

As expected, the coating deposited from the pure TiB_2 target is over-stoichiometric in boron content ($\text{TiB}_{3.1}$) due to the different sputter characteristics of Ti and B. Whereas B is sputtered mainly along with the target normal, Ti is sputtered along with a cosine function according to Neidhardt [53], leading to a deficiency in Ti content. Adding molybdenum into the coatings results in more stoichiometric coatings if a Mo content of ~ 7 at% is not exceeded. The progression from over- to under-stoichiometric thin films with increasing Mo content becomes even more apparent at the B/M ratio in **Figure 17 b**). An explanation for this behavior might be a different sputter behavior within the Mo-containing plasma compared to the only Ti and B containing one, due to the higher molecular weight and atomic size of Mo in comparison to Ti and B.

Highlighted are three compositions ($\text{TiB}_{3.1}$, $\text{Ti}_{0.94}\text{Mo}_{0.06}\text{B}_{1.94}$, and $\text{Ti}_{0.88}\text{Mo}_{0.12}\text{B}_{1.59}$) that will be investigated in more detail. These three coatings were selected for practical reasons, as they are deposited with only one target (less influences on the process), and their overall good properties are presented in the following two sections.

6.1.1 Structure and Morphology

SEM was used to determine the coating thickness and get a general impression of the morphology of the deposited coatings. The resulting cross sections of the thin films are shown in **Figure 18**. The overall thickness lies between 1.24 μm (see g) and 2.15 μm (see f), corresponding to a deposition rate of 20.66 nm/min and 35.75 nm/min. It must be considered that the coatings in b), d), and f) were produced by co-sputtering of two targets, which explains higher deposition rates. For films a) 1.45 μm , e) 1.50 μm , and c) 1.52 μm the thickness increased slightly for the Mo-containing sputter processes using only a single target.

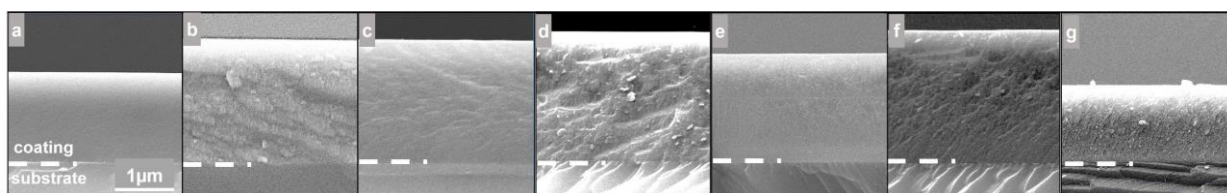


Figure 18: SEM fracture cross sections on Si substrates. All images were obtained using 10 kV voltage (FEGSEM Quanta 250); a) corresponds to coating $\text{TiB}_{3.1}$, b) to coating $\text{Ti}_{0.96}\text{Mo}_{0.04}\text{B}_{2.21}$ c) to coating $\text{Ti}_{0.94}\text{Mo}_{0.06}\text{B}_{1.94}$, d) to coating $\text{Ti}_{0.90}\text{Mo}_{0.10}\text{B}_{1.95}$, e) to coating $\text{Ti}_{0.88}\text{Mo}_{0.12}\text{B}_{1.59}$, f) to coating $\text{Ti}_{0.79}\text{Mo}_{0.21}\text{B}_{1.65}$ and g) to coating $\text{Ti}_{0.71}\text{Mo}_{0.29}\text{B}_{0.8}$

All thin films (a – g) obtain a very fine-grained structure and no typical columnar features are recognizable.

XRD measurements on Si-substrates were performed using the previously (chapter 5.4) described XRD system in Bragg-Brentano configuration to determine the crystal structure. The resulting diffractograms are presented in **Figure 19**.

By comparing the diffractogram of the pure $\text{TiB}_{3.1}$ thin film with the literature reference pattern, the crystal structure is identified to be $\alpha\text{-TiB}_2$ (SG 191). This coating shows a preferred orientation in the 001-direction, giving the first hint at a possible high hardness [55].

The general peak intensity decreases with increasing Mo content indicating a decrease in crystallinity, up to an amorphous state for the film with the highest Mo content. The peak positions are consistent with the $\alpha\text{-TiB}_2$ reference pattern. The films show a mixed orientation in 100- and 101-directions but do not show a 001-orientation with added Mo. The α -structure is retained even when alloying with Mo. No second phase, matching the $\alpha\text{-MoB}_2$ (SG 191) reference pattern occurs, which leads to the assumption that a solid solution between Mo and the TiB_2 is formed.

Most peaks are shifted slightly to the right. Residual stresses can explain this shift within the thin films or point defects such as vacancies and interstitials within the crystals of the thin films.

The small peaks between a 2θ -angle of 20° and 25° are not indicated, as well as the small peaks between 50° and 60° (except the 002-peak for $\text{TiB}_{3.1}$), as they are very likely measurement artifacts. Also not indicated is the peak at a 2θ -angle around 33° . This is the so-called “forbidden Si-peak” originating from the substrate.

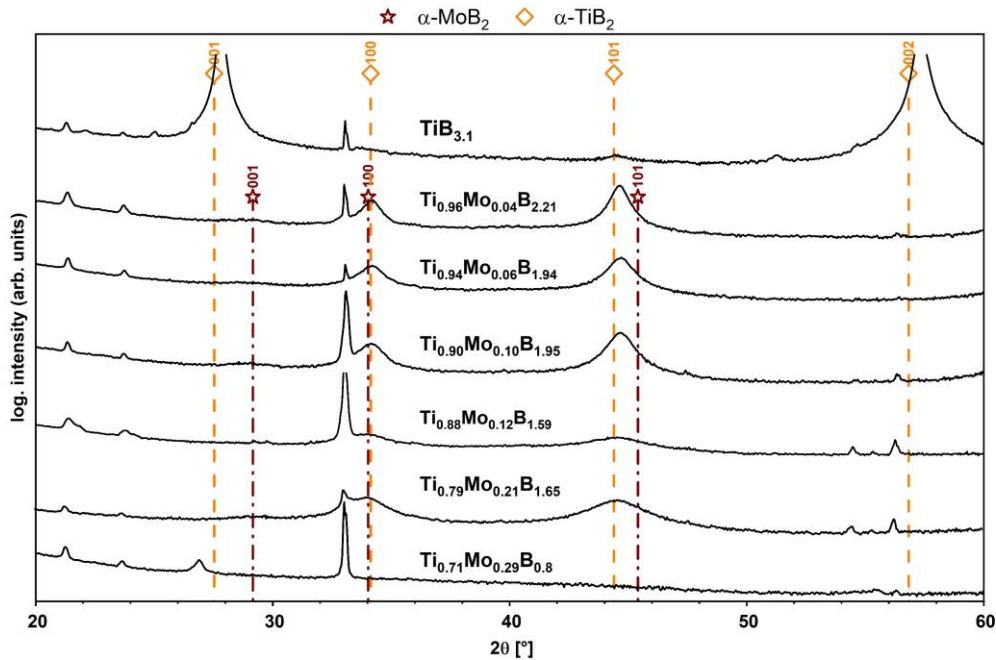


Figure 19: X-ray diffractograms of the deposited thin films with increasing Mo content from top to bottom. Indicated in orange are the reference positions of $\alpha\text{-TiB}_2$ peaks and the reference positions of $\alpha\text{-MoB}_2$ peaks in dark red.

To conclude the investigations on the preliminary depositions, the mechanical properties were determined, and the results are presented in the following chapter.

6.1.2 Mechanical Properties

The mechanical properties hardness H and indentation modulus E were investigated using nanoindentation and calculated according to the method of Oliver and Pharr [65]. All measurements were carried out on austenite substrates. The propagation of H (blue) and E (pink) are plotted over the Mo content displaying the influence of alloying, shown in **Figure 20**.

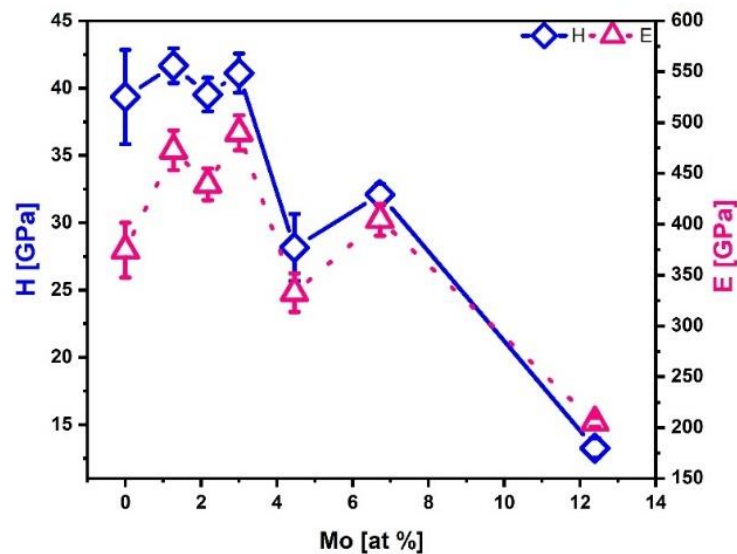


Figure 20: The mechanical properties hardness (H) and indentation modulus (E) are plotted over the Mo content. Hardness values are indicated by the blue boxes, and the values for the indentation modulus by the pink triangles.

For the $\text{TiB}_{3.1}$ thin film, a hardness of 39.35 ± 3.5 GPa and an indentation modulus of 374.38 ± 26.97 GPa was determined. Up to a Mo content of around 4 at %, the hardness ranges between 39 GPa and nearly 42 GPa (peaking at 41.67 ± 1.29 GPa), then decreases by more than 10 GPa to 28.16 ± 2.49 GPa for the film with the composition $\text{Ti}_{0.88}\text{Mo}_{0.12}\text{B}_{1.59}$. There is a slight increase of H , followed by another step decrease for the coating with the highest Mo content. The drop in hardness for the thin film composition $\text{Ti}_{0.94}\text{Mo}_{0.06}\text{B}_{1.94}$ is caused by too high residual stresses in the film. This was expected as the film was spalling off the substrate directly after coating. For $\text{Ti}_{0.88}\text{Mo}_{0.12}\text{B}_{1.59}$, the reduced hardness can be explained by the amorphous structure.

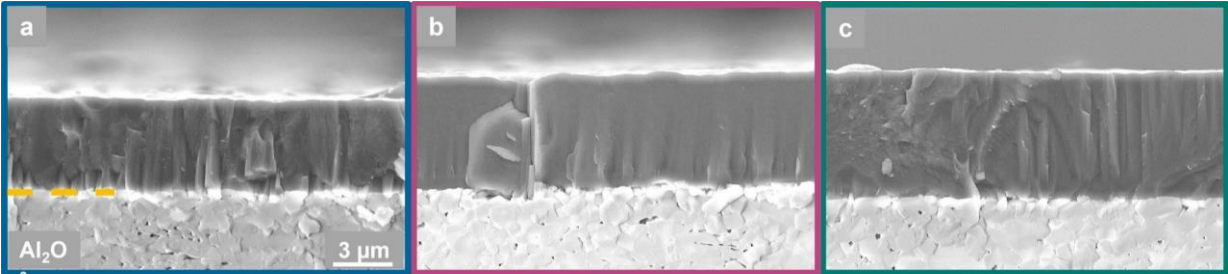
The progression of the indentation modulus is similar to the hardness over the increasing Mo content. With 332.75 ± 18.79 GPa, the lowest value was measured for $\text{Ti}_{0.88}\text{Mo}_{0.12}\text{B}_{1.59}$ and the highest for 489.94 ± 17.17 GPa for the thin film with composition $\text{Ti}_{0.90}\text{Mo}_{0.10}\text{B}_{1.95}$.

The next part of this thesis deals with three thin film states picked out for a more detailed investigation.

6.2 Detailed Investigation of $\text{TiB}_{3.1}$, $\text{Ti}_{0.94}\text{Mo}_{0.06}\text{B}_{1.94}$ and $\text{Ti}_{0.88}\text{Mo}_{0.12}\text{B}_{1.59}$ thin films

Three composition states ($\text{TiB}_{3.1}$, $\text{Ti}_{0.94}\text{Mo}_{0.06}\text{B}_{1.94}$, and $\text{Ti}_{0.88}\text{Mo}_{0.12}\text{B}_{1.59}$) have been redeposited for a more detailed investigation. The deposition parameters were not changed except for the coating time ($\sim 300 - 320$ min) to derive coatings with thicknesses of about $5 \mu\text{m}$. Technical substrates (TiAl6V4) and polycrystalline Al_2O_3 substrates experiments have been coated in addition to the formerly used substrates. Structure and morphology have been investigated using SEM, TEM, and XRD. Nanoindentation was used for the determination of the mechanical properties and in-situ micromechanical testing to determine the fracture toughness. The thermal behavior of the thin films was analyzed by vacuum annealing experiments and dynamic oxidation. To conclude the measurements, the erosion resistance was investigated. In the following chapters, the results are presented and discussed.

6.2.1 Structure and Morphology

SEM cross-sections on polycrystalline Al_2O_3 are shown in **Figure 21**. All coatings obtain a nanocrystalline, dense morphology. Columnar film growth cannot be seen in 20 a-c) as the resolution of the SEM is too low. The morphology visible in a-c) originates from the fracture morphology of the substrate. 

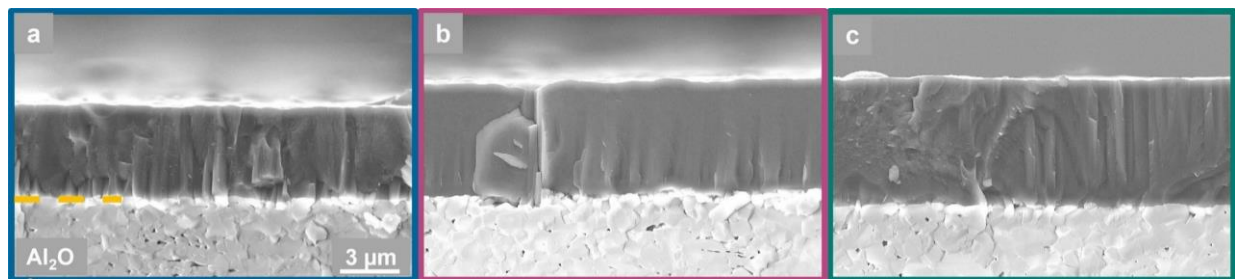


Figure 21 SEM images on Al_2O_3 substrate, cross sections, a) $\text{TiB}_{3.1}$, b) $\text{Ti}_{0.94}\text{Mo}_{0.06}\text{B}_{1.94}$ c) $\text{Ti}_{0.88}\text{Mo}_{0.12}\text{B}_{1.59}$

Due to a higher resolution TEM investigation has been conducted to gain more detailed information on the morphology. The results are presented in **Figure 22**, **Figure 23** and **Figure 24**.

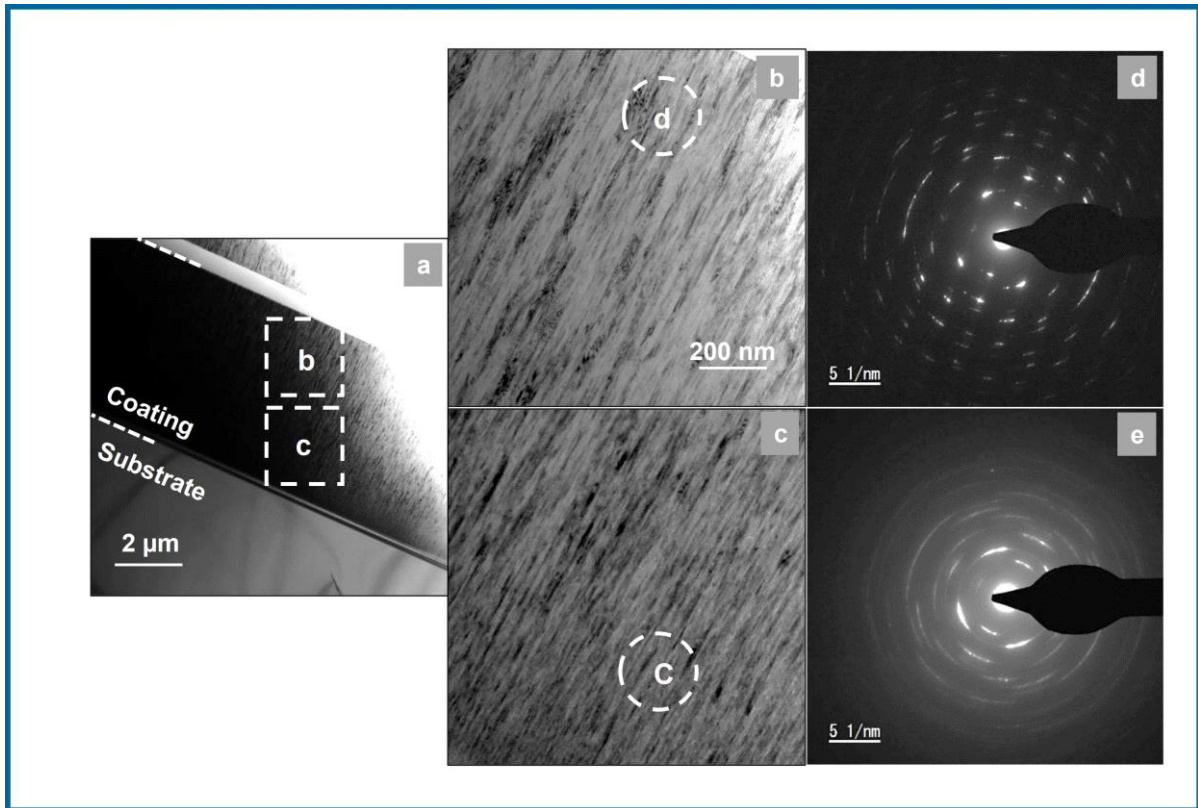


Figure 22 TEM images $TiB_{3.1}$, a) overview, b) bright field close to surface, c) bright field close to substrate, d) SAED close to the surface, and e) SAED close to the substrate

The TEM cross section in Figure 22a) clearly shows the columnar, fine-crystalline growth of the thin film. For further insight, two spots, one close to the surface 22b) and one close to the substrate 22c), were chosen, and bright field images with higher magnification were taken. An increasing column size with increasing distance from the substrate was revealed. SAED diffractograms for both regions were taken 22d) close to surface and 22e) close to substrate. A highly textured coating is present in the region close to the substrate. At the surface near position, the SAED diffractogram resembles almost single-crystalline within the used aperture, showing preferred orientation within the thin film.

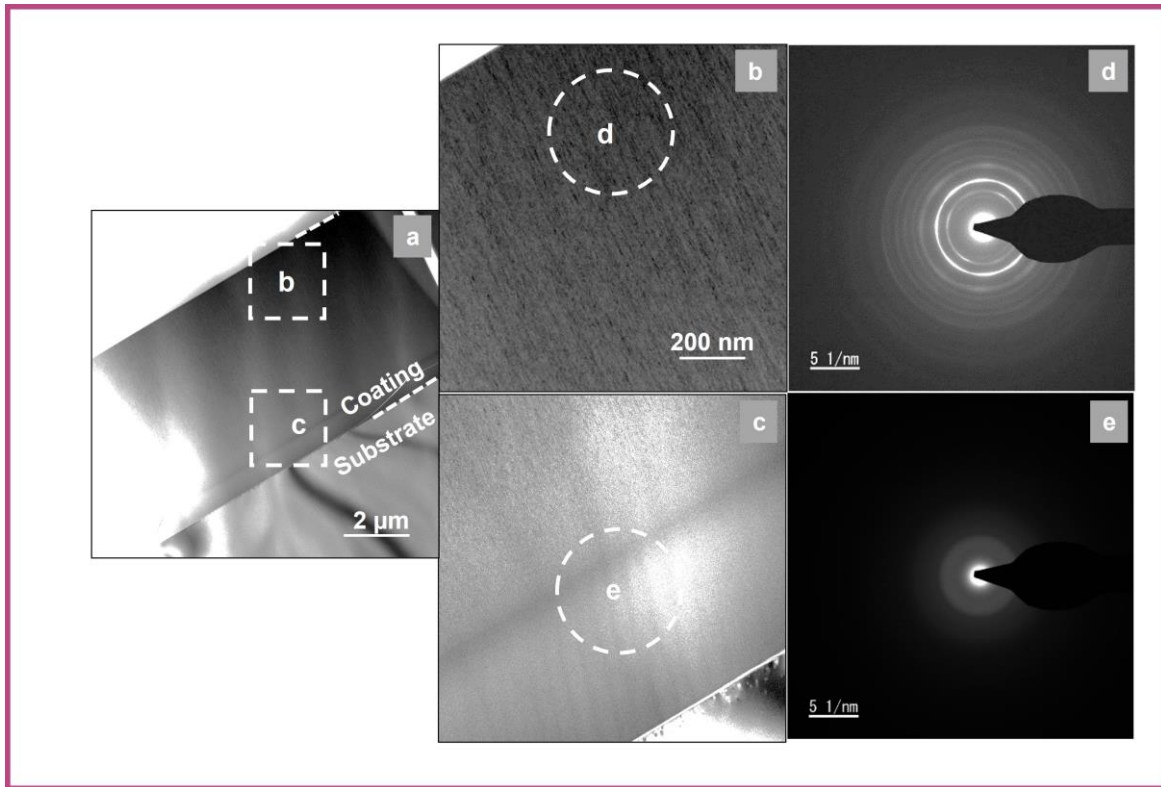


Figure 23: TEM images $Ti_{0.94}Mo_{0.06}B_{1.94}$, a) overview, b) bright field close to surface, c) bright field close to substrate d) SAED close to surface, e) SAED close to the substrate

A cross-section of the analyzed probe is given in 23a) indicating the two areas looked at more in detail. TEM investigations on $Ti_{0.94}Mo_{0.06}B_{1.94}$ revealed a visible columnar film growth, broadening from the substrate near region 23c) to the surface 23b). In 23c), a transition within the coating is recognizable. The substrate near region 23e) exhibits an amorphous structure, whereas the surface near region 23d) is crystalline with a slightly preferred orientation.

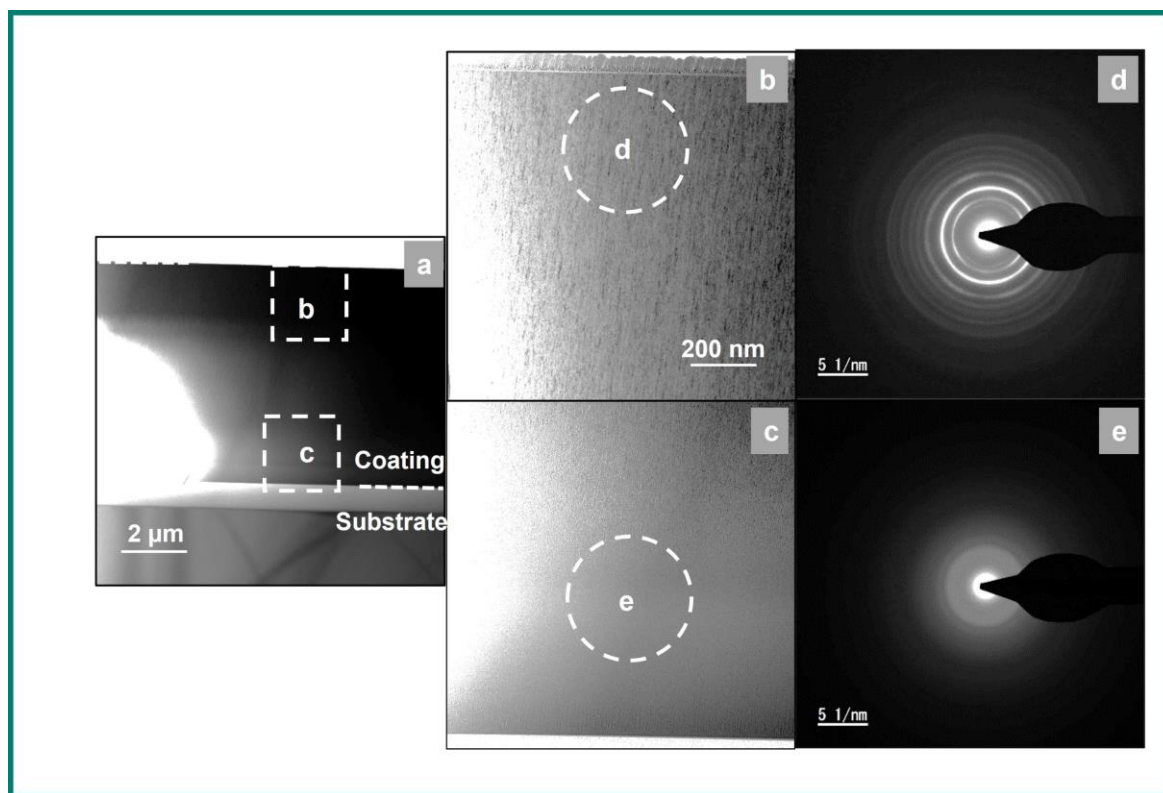


Figure 24: TEM images $Ti_{0.88}Mo_{0.12}B_{1.59}$, a) overview, b) bright field close to surface, c) bright field close to substrate d) SAED close to surface, e) SAED close to substrate

The coating with the highest Mo content in this series also exhibits columnar growth with decreasing column size from substrate to the surface 24(a-c) and extremely small crystallite size. A transition between structure at the substrate near region 24c) and the surface near region 24b) is confirmed by SAED measurements. The diffractogram at the substrate near 24e) position reveals an amorphous structure. Closer to the surface, the thin film is crystalline with preferred crystal orientation.

All investigated film systems show a fine columnar structure, typical for films grown by PVD. Alloying with Mo decreases crystallite size compared to the already nano/fine-crystalline $TiB_{3.1}$ thin film. The amorphous region observed for both Mo containing coatings will for sure influence the properties of the coatings. An explanation for the formation of this amorphous “layer” might be the deposition process itself, where oxide impurities originating from the residual oxygen within the target material and/or oxidized target surfaces could not be fully removed by pre-sputtering could hinder the growth of a crystalline film.

X-ray diffraction analysis was performed on austenite substrates to determine the crystal structure and orientation of the thin films. These experiments were carried out using the Bragg-Brentano configured instrument, already described in chapter 5.4 and the results are presented below.

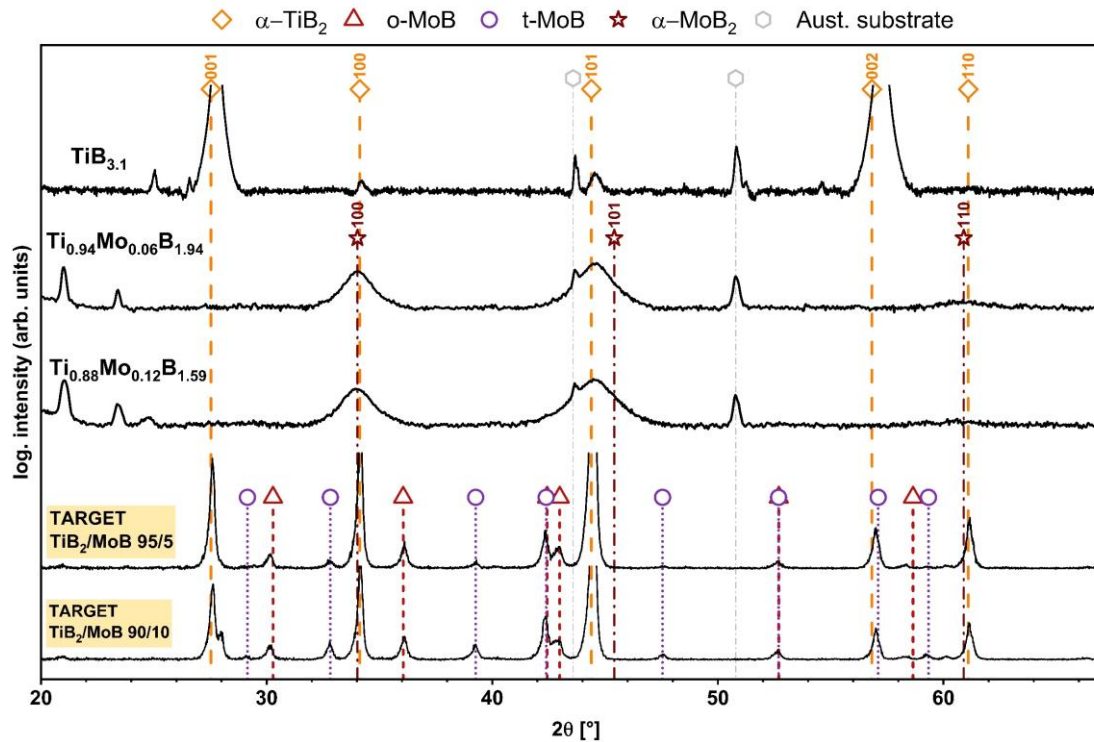


Figure 25: XRD diffractogram of the three coating systems, measured on austenite substrates and the reference diffractograms of the used targets for the Mo containing coatings. The reference pattern for the austenite substrate is indicated by light grey symbols, α -TiB₂ in orange, α -MoB₂ in dark red, t-MoB (tetragonal) in violet, and o-MoB (orthorhombic) in light red.

The target diffractograms serve as a comparison to the diffractograms derived by the measurements of the deposited coatings. α -TiB₂ and t-MoB, and o-MoB are identified, which originate from the two materials mixed to produce the target. In addition to the target diffractograms, the diffractograms of the deposited coatings TiB_{3.1}, Ti_{0.94}Mo_{0.06}B_{1.94}, and Ti_{0.88}Mo_{0.12}B_{1.59} are shown in **Figure 25**.

TiB_{3.1} crystallizes in the α -TiB₂ (SG191) structure with preferred orientation in the 001-direction, as already shown for this coating in **chapter 6.1.1**. As for Mo containing thin films, a drastically decreasing peak intensity and no 001-orientation are present. The mixed orientation of 100 and 101-directions is identified through comparison with reference peak positions for α -TiB₂ (SG191). Peak positions indicative of the presence of α -MoB₂ (SG191) structure are only moderately concordant, which is consistent with formerly presented results. None of the two MoB-phases is found in the deposited coatings, leading to the assumption that Mo is in a solid solution within the TiB₂-phase.

The peaks between 20 ° and 26 ° are not indicated as they probably result from measurement fragments.

Following the structural characterization is the investigation of the mechanical properties.

6.2.2 Mechanical Properties

Nanoindentation was used to determine the hardness and the indentation modulus. The results are displayed in **Figure 26 a)**, where they are plotted over the Mo content. The H^3/E^2 ratio is shown in Figure 26 b). All measurements have been performed on austenite substrates.

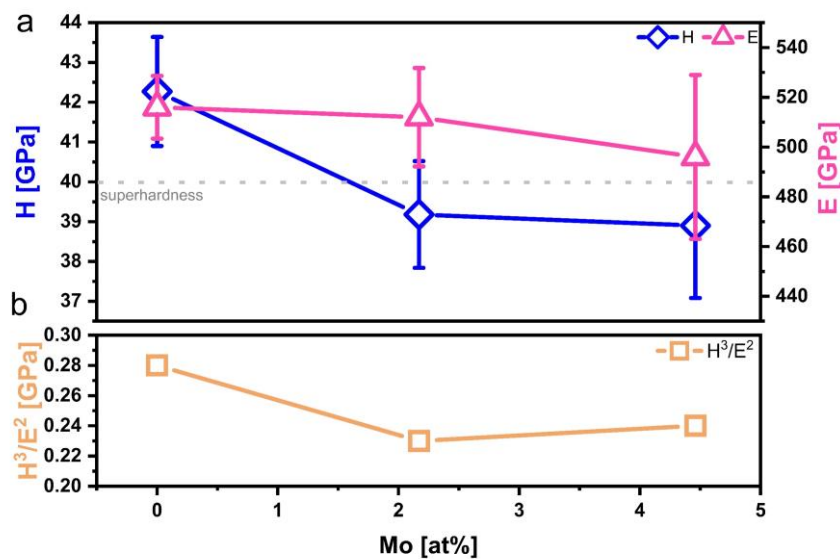


Figure 26: Mechanical properties plotted over the Mo content. a) Hardness H in blue, Indentation modulus E in pink, b) H^3/E^2 ratio in light orange

The highest hardness was measured for the $TiB_{3.1}$ coating with 42.27 ± 1.37 GPa, slightly decreasing to 39.18 ± 1.34 GPa for $Ti_{0.94}Mo_{0.06}B_{1.94}$ and to 38.90 ± 1.82 GPa for $Ti_{0.88}Mo_{0.12}B_{1.59}$. The indentation moduli range between 516 ± 12.62 GPa and 496 ± 32.98 GPa from $TiB_{3.1}$ to $Ti_{0.88}Mo_{0.12}B_{1.59}$. Looking at the H^3/E^2 ratio, the highest value (0.28) belongs to $TiB_{3.1}$ and decrease slightly with for the Mo containing films.

Overall, the measured H values lie very close to each other, with a maximum difference of ~ 3 GPa, leading to the conclusion that alloying with Mo does not have a major influence on the hardness. The outstanding high hardness, which is typical for TiB_{2+z} and a beneficial characteristic of this material system, is confirmed in this work, as the deposited $TiB_{3.1}$ thin film exceeds the level of super-hardness (40 GPa). Furthermore, the goal to preserve a high hardness,

even though alloying with Mo, is reached, as the H values for the two Mo containing thin films, still ranges close to this level of super-hardness. The addition of molybdenum, that is accompanied with a decrease in grain size (shown in chapter 6.2.1), acts for sure as a positive effect towards, maintaining/exhibiting high hardness values. In contrast, the transition from a preferred 001-crystal orientation for TiB₃.1 to a mixed 100- and 101- orientation, is certainly responsible for the decrease in hardness. Secondly, the amorphous region close to the substrate, shown by TEM investigations affects the mechanical properties for sure. A similar linear-elastic behavior of all three coatings is assumed, as the indentation moduli (E) exhibits only small differences between the three coatings. The resistance to the onset of plastic deformation is described by the H^3/E^2 ratio, which shows only minor differences for all investigated material systems.

In order to obtain a complete overview of all mechanical properties of the systems, micro-mechanical testing followed to determine the fracture toughness.

6.2.3 Fracture Toughness

The intrinsic fracture toughness of the three coatings ($\text{TiB}_{3.1}$, $\text{Ti}_{0.94}\text{Mo}_{0.06}\text{B}_{1.94}$ and $\text{Ti}_{0.88}\text{Mo}_{0.12}\text{B}_{1.59}$) was measured using in-situ micro-cantilever bending tests. The cantilevers were prepared by FIB milling on austenite substrates. Measurements of the geometry (fracture cross-sections) were done by SEM, and the calculation of the fracture toughness was done following the equations given in **Chapter 5.5** for at least five cantilevers per composition.

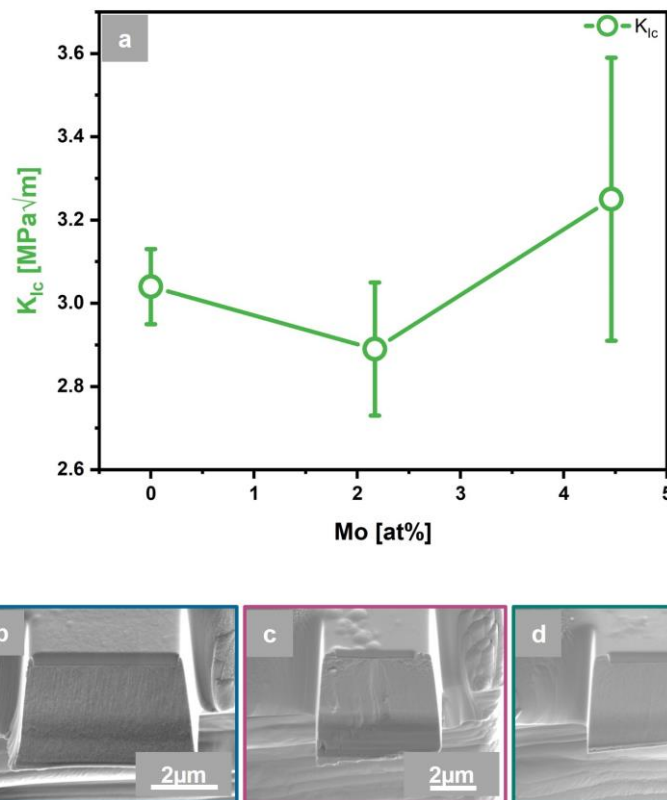


Figure 27: a) Fracture toughness over Mo content and b-d) the fracture cross-sections

The fracture toughness for $\text{TiB}_{3.1}$ amounts to $3.04 \pm 0.09 \text{ MPa}\sqrt{\text{m}}$, for $\text{Ti}_{0.94}\text{Mo}_{0.06}\text{B}_{1.94}$ $2.89 \pm 0.16 \text{ MPa}\sqrt{\text{m}}$, and for $\text{Ti}_{0.88}\text{Mo}_{0.12}\text{B}_{1.59}$ $3.25 \pm 0.34 \text{ MPa}\sqrt{\text{m}}$. **Figure 27** a) displays the values for K_{IC} over the increasing Mo content. The values range around $3 \text{ MPa}\sqrt{\text{m}}$ with only minor differences, making it difficult to make a concrete statement about the influence of Mo on fracture toughness. Looking at the thin film containing the highest amount of Mo, a slight increase in the K_{IC} value possibly indicates that the predictions of alloying Mo into TiB_{2+z} increases ductility according to the DFT calculations. However, the statistical error must be taken into consideration. Therefore, the results are somewhat inconclusive. When comparing the measured values with some of the literature, a dependence of K_{IC} and the B content of TiB_{2+z}

thin films was shown, with decreasing K_{IC} values for increasing B content [52]. The values obtained in this study do range in the same order of magnitude shown for TiAlN (2.7 – 3.0 $\text{MPa}\sqrt{\text{m}}$) [76] and $\text{W}_{0.74}\text{Ta}_{0.26}\text{B}_{1.87}$ (3.0 $\text{MPa}\sqrt{\text{m}}$) [16]. Compared with TiN (1.9 $\text{MPa}\sqrt{\text{m}}$) [76], all three coating systems investigated in the present study obtain a higher fracture toughness and therefore a less brittle character is assumed. Exemplary, one fracture cross-section for each thin film composition is shown in Figure 27 b-d).

Possible reasons for the deviations in the present measuring series are the FIB preparation of the cantilevers, as re-deposition is hardly avoidable. Additionally, the amorphous region present in both Mo-containing thin films impacts the fracture behavior, but its extent is unknown as no other Mo-containing thin films were investigated during this study in terms of comparison.

6.2.4 Erosion tests

A test setup according to ASTM G76 has been used to determine the solid particle erosion resistance. Tests were conducted with tilt angles of 30° and 90° of the samples in perspective to the nozzle. Before testing the three coating states, the system has been calibrated regarding the amount of abrasive flowing through the nozzle, and an uncoated blank sample (TiAl6V4) has been eroded. For the erosion test, the three coating systems were deposited onto already mentioned TiAl6V4 substrates (25 x 25 mm).

A pretest for 30 seconds at both angles (30° and 90°) was conducted for a first impression of the material's behavior. All thin films have shown a higher resistance against solid particle erosion at 30° and immediate material loss at 90° ; therefore, only tests at an angle of 30° have been performed. The erosion time was increased in 30 or 60 second steps (depending on the sample), and after each increment, the sample was weighted on an analytical balance, and under an optical light microscope, the surface of the sample was checked for any erosion craters. SPE crater development progression of $\text{TiB}_{3.1}$, $\text{Ti}_{0.94}\text{Mo}_{0.06}\text{B}_{1.94}$ and $\text{Ti}_{0.88}\text{Mo}_{0.12}\text{B}_{1.59}$ is shown in **Figure 28 a-c)** respectively.

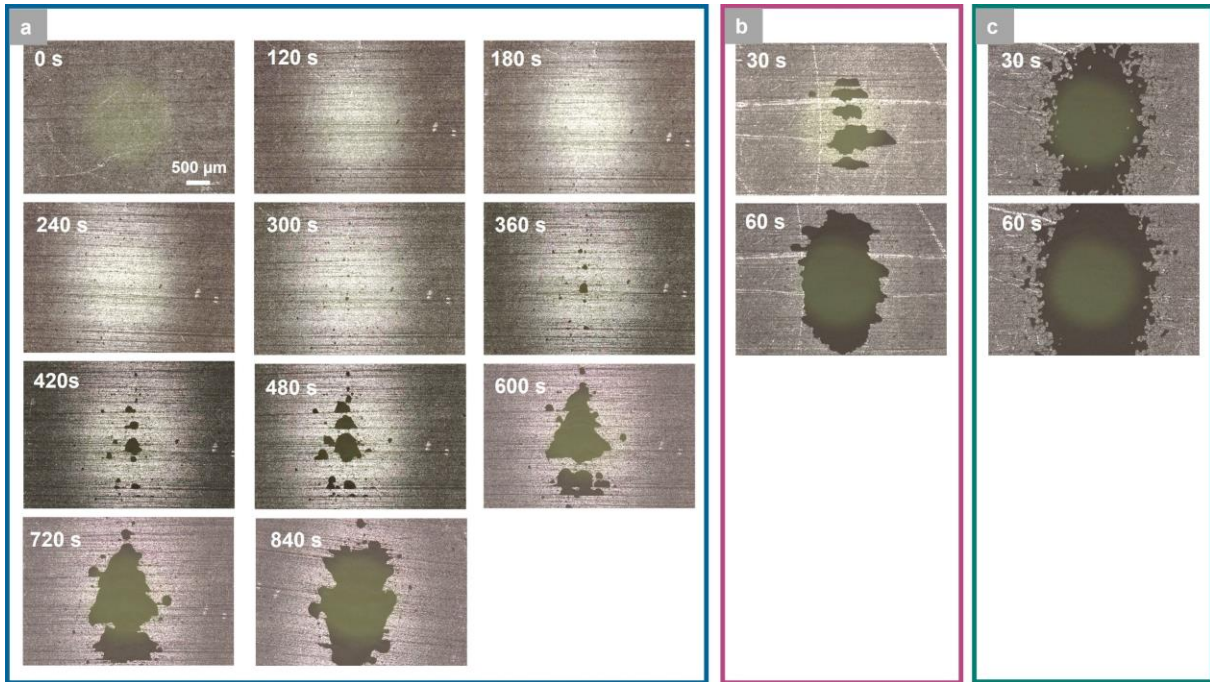


Figure 28: Progression of SPE at 30 ° for a) $TiB_{3.1}$. b) $Ti_{0.94}Mo_{0.06}B_{1.94}$ and c) $Ti_{0.88}Mo_{0.12}B_{1.59}$

$TiB_{3.1}$ shows the first signs of material loss between 300 and 360 seconds (Figure 28 a). Before that, the impacting particles do not cause any change on the coating surface. This behavior is also confirmed by looking at the mass loss over time in **Figure 29**, with the blue and violet circles belonging to $TiB_{3.1}$. Due to the prior promising result, more than one sample has been eroded on TiAl6V4 (A12, A13, A16) and one on the QRS substrate. All curves show minimal mass loss up to 360 seconds, with a slight increase up to around 600 seconds, followed by severe mass loss. The calculated erosion rate for $TiB_{3.1}$ amounts to $3.2 \mu\text{g/g}$. The sudden increase in mass loss of the coating is due/caused by the fatigue of the interface between coating and substrate.

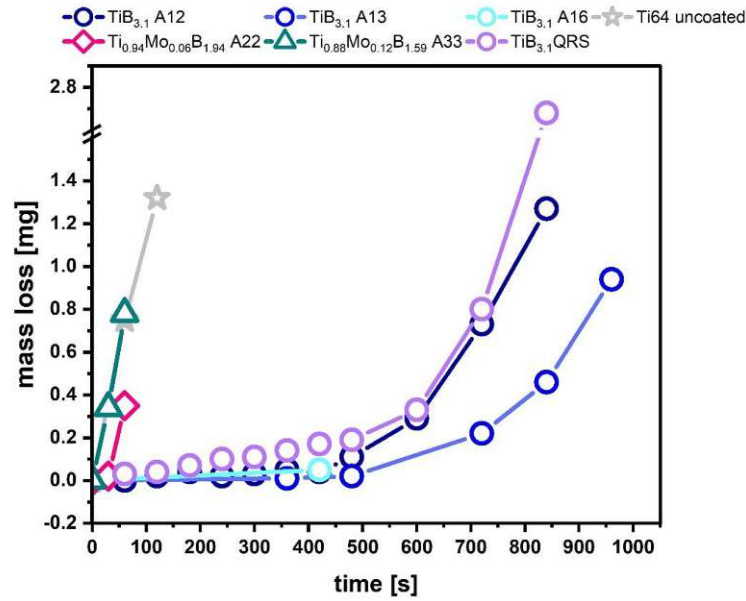


Figure 29: Mass loss in mg over time during erosion experiments at impact angle 30° for the uncoated substrate TiAl6V4 (grey stars), TiB_{3,1} (blue circles) and the Mo containing thin films pink boxes and green triangles

Ti_{0.94}Mo_{0.06}B_{1.94} and Ti_{0.88}Mo_{0.12}B_{1.59} exhibit damage at 30 seconds of erosion time (see Figures 26 b) and c). The mass loss over time shows a similar progression for both coatings (pink squares and green triangles) in Figure 27. The calculated erosion rate for Ti_{0.94}Mo_{0.06}B_{1.94} and Ti_{0.88}Mo_{0.12}B_{1.59} amount to 20 $\mu\text{g/g}$ and 340 $\mu\text{g/g}$, respectively.

The poor erosion resistance of the two Mo alloyed thin films is attributed to the amorphous part, which has been described in Chapter 6.2.1. Due to this inconvenience, the adhesion of the coating onto the substrate is negatively influenced. Hence, a clear statement about the positive or negative influence of Mo on the resistance against SPE is challenging to make.

6.2.5 Thermal Properties

Vacuum annealing experiments from 500 °C to 800 °C for 1 hour and 10 hours each were done on polycrystalline Al₂O₃ substrates. To gain insight into any phase transitions/formations that might occur, XRD measurements were performed for each coating in the as-deposited state and after each annealing step, as phase stability is a decisive factor for consistent material properties at elevated temperatures.

Exemplary two measurement series will be described here. The residual XRD diffractograms can be found in **Appendix A**.

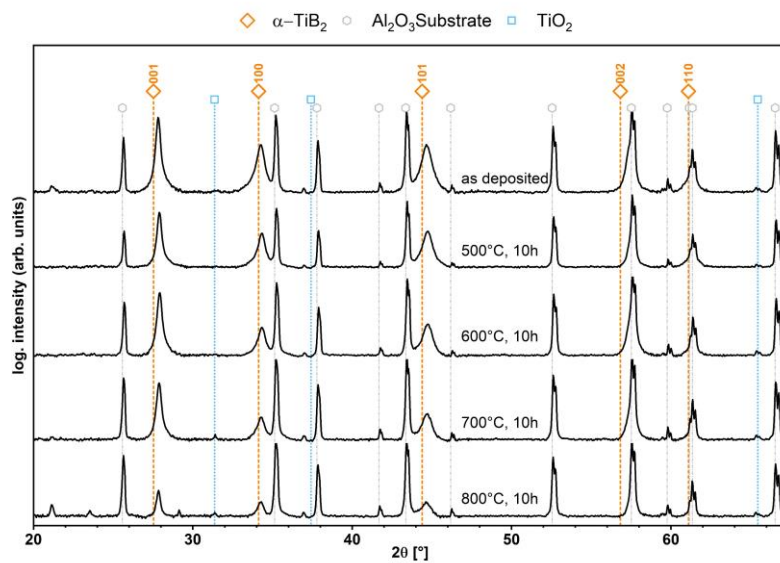


Figure 30: Resulting XRD diffractograms for the 10 h annealing of TiB_{3.1} in the as deposited state and after the annealing at 500, 600, 700 and 800 °C.

Figure 30 shows the diffractograms for TiB_{3.1} in the as deposited state and the diffractograms received after annealing for 10 hours at 500, 600, 700, and 800 °C from top to bottom. When comparing the peaks with the reference pattern, the α -TiB₂ structure can be identified. The thin film shows a mixed orientation with a preference for the 001-orientation. TiO₂ is also found to a minimal extent. During annealing, the peak intensity for the TiB₂ decreases with increasing temperatures, and the peak intensity for TiO₂ slightly increases. Residual stresses cause the peak shift regarding the TiB₂ reference positions within the coating or point defects, such as vacancies or interstitials. The small amount of TiO₂ already present in the as deposited state, originates most likely from the residual oxygen within the target. Overall, TiB₂ exhibits phase stability during vacuum annealing up to 800 °C for 10 h.

For the Mo containing coatings the same experiments were done. The results for the annealing of the thin film with the highest Mo content for the 10-hour annealing series are presented in **Figure 31**.

In accordance with the previously presented XRD results $Ti_{0.88}Mo_{0.12}B_{1.59}$ does not show a preferred orientation in the 001-direction but a mixed orientation in the 100 and 101-direction of the identified α - TiB_2 structure. The peak shape changes, starting at 700 °C from a broad to a more pointed form, indicating an increase in grain size.

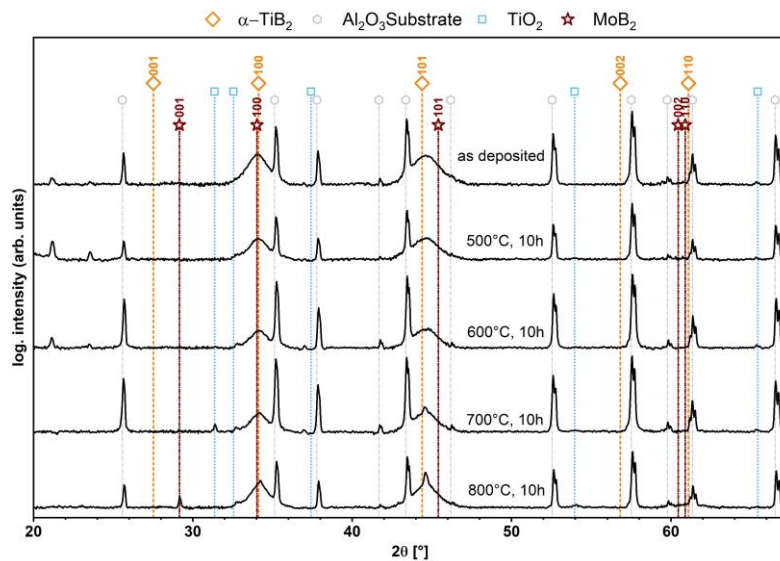


Figure 31: Resulting XRD diffractograms for the 10 h annealing of $Ti_{0.88}Mo_{0.12}B_{1.59}$ in the as deposited state and after the annealing at 500, 600, 700 and 800 °C.

TiO_2 is again present from the as deposited state, and its peak intensities do increase slightly with higher annealing temperatures. Mo alloying does not influence the structural stability at elevated temperatures up to 700 °C. At 800 °C, a small peak at $2\theta \sim 29^\circ$ forms that belongs to the 001-oriented α - MoB_2 structure, indicating the start of the separation of the solid solution, limiting the application temperature for such coatings.

The overall outcome of the present work is summarized in the following conclusions.

7. Conclusions

The aim of the present thesis was to study the influence of Mo on the structure and fracture-mechanical properties of TiB_{2+z} thin films manufactured by PVD. To reduce the poor fracture toughness and inherent brittleness of the TiB_2 system, DFT calculations suggest alloying with a more ductile material, in this case, MoB_2 was proposed to be a promising candidate to fulfill these requirements.

TiB_{2+z} and ternary $\text{Ti}_{1-x}\text{Mo}_x\text{B}_{2+z}$ thin films were prepared using the DC magnetron sputter deposition technique. For pre-screening, four targets (TiB_2/C 99/1 mol%, TiB_2/MoB 95/5 mol%, TiB_2/MoB 90/10 mol%, TiB_2/MoB 80/20 mol%) were either sputtered alone or co-sputtered to gain a broad spectrum of compositions. After investigating these thin films using SEM, XRD, and Nanoindentation, three states ($\text{TiB}_{3.1}$, $\text{Ti}_{0.94}\text{Mo}_{0.06}\text{B}_{1.94}$, and $\text{Ti}_{0.88}\text{Mo}_{0.12}\text{B}_{1.59}$) were chosen for further and more detailed investigations. In addition to SEM, XRD and Nanoindentation, TEM, in-situ cantilever bending experiments, erosion, and vacuum annealing experiments were carried out.

It was found that increasing the Mo content leads to an increase in Ti and a decrease in B content, producing more stoichiometric thin films. All coatings exhibit a nano-crystalline α - AlB_2 structure and morphology. As no MoB or MoB_2 phases in the as-deposited thin films are detected, we can assume that a solid solution within the ternary system is formed. All coatings exhibit thermal stability in vacuum up to 800 °C for 10 h, where the first signs of a second phase appeared for Mo containing thin films. The mechanical properties H and E decreased with increasing Mo content, from $H = 42.27 \pm 1.37$ GPa to $H = 38.9 \pm 1.82$ GPa and $E = 516 \pm 13$ GPa to $E = 496 \pm 33$ GPa from $\text{TiB}_{3.1}$ to $\text{Ti}_{0.88}\text{Mo}_{0.12}\text{B}_{1.59}$. Whereas the fracture toughness remained constant at around 3.0 $\text{MPa}\sqrt{\text{m}}$ and then increased slightly to 3.25 ± 0.34 $\text{MPa}\sqrt{\text{m}}$. During the erosion tests, $\text{TiB}_{3.1}$ exhibits excellent resistance against SPE.

To sum it up, this study shows the influence of Mo on the structure, the mechanical and fracture-mechanical properties of TiB_{2+z} thin films, and the predictions made by DFT calculations are strongly supported by the results of the present work. Overall, Mo is a suitable candidate for the improvement of fracture toughness while simultaneously maintaining the other desirable mechanical properties of TiB_{2+z} .

Appendix A

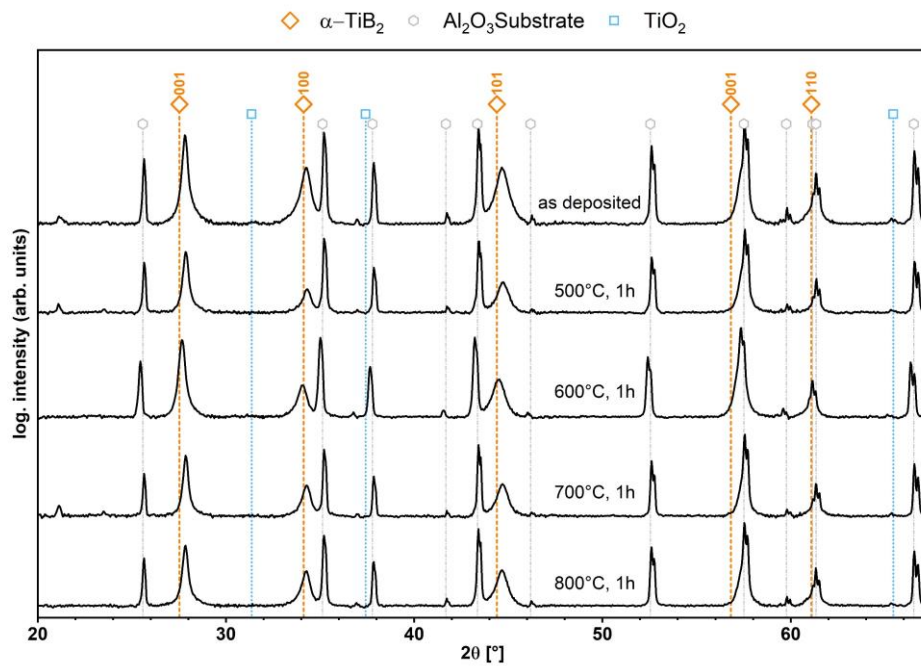


Figure 32: Resulting diffractograms of $TiB_{3.1}$ in the as deposited state and after annealing for 1 h at 500, 600, 700 and 800 °C

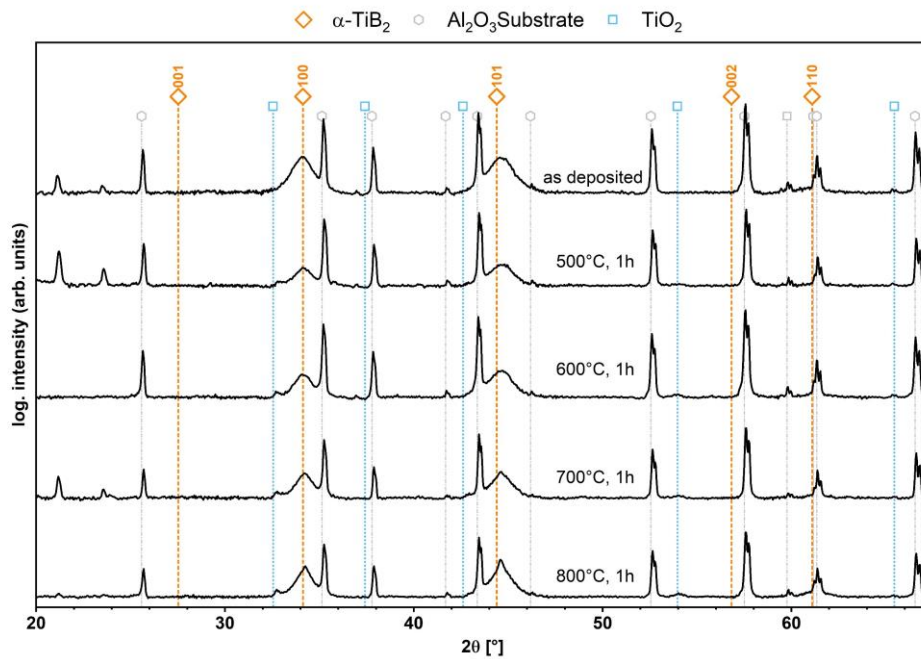


Figure 33: Resulting diffractograms of $Ti_{0.94}Mo_{0.06}B_{1.94}$ in the as deposited state and after annealing for 1 h at 500, 600, 700 and 800 °C

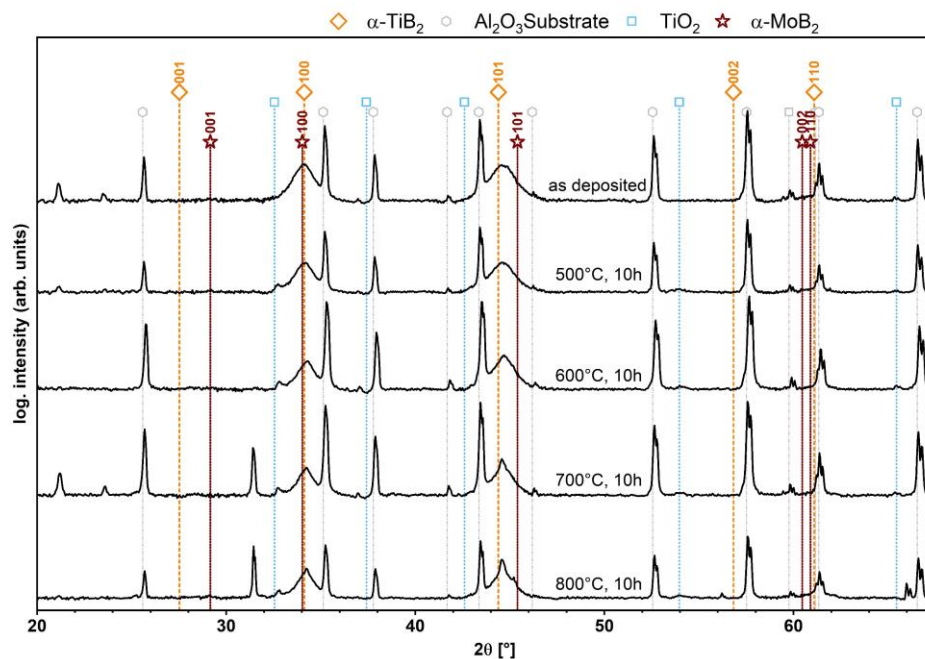


Figure 34: Resulting diffractograms of $Ti_{0.94}Mo_{0.06}B_{1.94}$ in the as deposited state and after annealing for 10 h at 500, 600, 700 and 800 °C

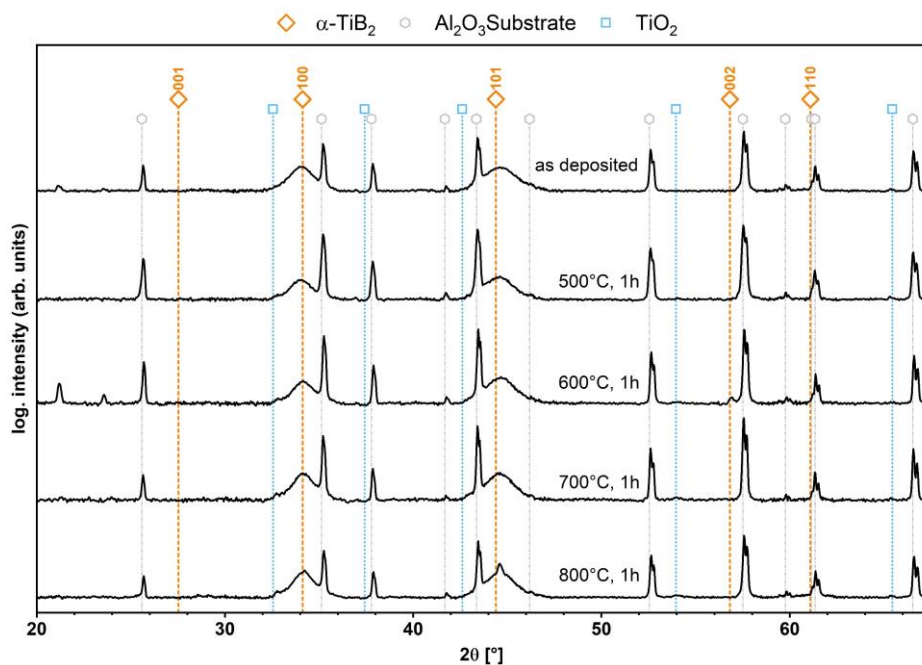


Figure 35: Resulting diffractograms of $Ti_{0.88}Mo_{0.12}B_{1.59}$ in the as deposited state and after annealing for 10 h at 500, 600, 700 and 800 °C

Literature

Literatur

- [1] P. M. Martin, *Handbook of deposition technologies for films and coatings: Science, applications and technology*, 3. Aufl. Norwich, N.Y., Oxford: William Andrew; Elsevier Science, 2009. [Online]. Verfügbar unter:
<http://gbv.ebib.com/patron/FullRecord.aspx?p=566654>
- [2] E. Bousser, L. Martinu und J. E. Klemberg-Sapieha, „Solid particle erosion mechanisms of protective coatings for aerospace applications“, *Surface and Coatings Technology*, Jg. 257, S. 165–181, 2014, doi: 10.1016/j.surfcoat.2014.08.037.
- [3] K. Bobzin, N. Bagcivan, P. Immich, C. Pinero, N. Goebbels und A. Krämer, „PVD – Eine Erfolgsgeschichte mit Zukunft“, *Mat.-wiss. u. Werkstofftech.*, Jg. 39, Nr. 1, S. 5–12, 2008, doi: 10.1002/mawe.200700252.
- [4] K. S. Sree Harsha, *Principles of physical vapor deposition of thin films*, 1. Aufl. Amsterdam: Elsevier, 2006. [Online]. Verfügbar unter:
<http://site.ebrary.com/lib/alltitles/docDetail.action?docID=10179288>
- [5] M. Ohring, *Materials Science of Thin Films*, 2. Aufl. s.l.: Elsevier textbooks, 2001. [Online]. Verfügbar unter: <http://gbv.ebib.com/patron/FullRecord.aspx?p=294629>
- [6] D. M. Mattox, *Handbook of physical vapor deposition (PVD) processing*, 2. Aufl. Amsterdam, Oxford: Elsevier; William Andrew, 2010.
- [7] K. Bobzin, „High-performance coatings for cutting tools“, *CIRP Journal of Manufacturing Science and Technology*, Jg. 18, S. 1–9, 2017, doi: 10.1016/j.cirpj.2016.11.004.
- [8] C. Mitterer, „Borides in Thin Film Technology“, *Journal of Solid State Chemistry*, Jg. 133, Nr. 1, S. 279–291, 1997, doi: 10.1006/jssc.1997.7456.
- [9] C. Mitterer, „PVD and CVD Hard Coatings“ in *Comprehensive hard materials: Volume 1-3: Hardmetals, ceramics, super hard materials*, C. E. Nebel, D. Mari, L. LLanes und V. K. Sarin, Hg., Amsterdam, Waltham, Heidelberg: Elsevier, 2014, S. 449–467, doi: 10.1016/B978-0-08-096527-7.00035-0.
- [10] V. Moraes *et al.*, „Thermally stable superhard diborides: An ab initio guided case study for V-W-diboride thin films“, *Acta Materialia*, Jg. 186, S. 487–493, 2020, doi: 10.1016/j.actamat.2020.01.014.
- [11] J. G. Ryan, S. Roberts, G. J. Slusser und E. D. Adams, „The preparation and characterization of titanium boride films“, *Thin Solid Films*, Jg. 153, 1-3, S. 329–339, 1987, doi: 10.1016/0040-6090(87)90193-3.
- [12] P. H. Mayrhofer, C. Mitterer, J. G. Wen, J. E. Greene und I. Petrov, „Self-organized nanocolumnar structure in superhard TiB₂ thin films“, *Appl. Phys. Lett.*, Jg. 86, Nr. 13, S. 131909, 2005, doi: 10.1063/1.1887824.
- [13] B. Bakhit *et al.*, „Improving the high-temperature oxidation resistance of TiB₂ thin films by alloying with Al“, *Acta Materialia*, Jg. 196, S. 677–689, 2020, doi: 10.1016/j.actamat.2020.07.025.
- [14] V. Moraes *et al.*, „Ab initio inspired design of ternary boride thin films“ (eng), *Scientific reports*, Jg. 8, Nr. 1, S. 9288, 2018, doi: 10.1038/s41598-018-27426-w.
- [15] P. Malinovskis, J. Palisaitis, P. O. Å. Persson, E. Lewin und U. Jansson, „Synthesis and characterization of MoB_{2-x} thin films grown by nonreactive DC magnetron

- sputtering“, *Journal of Vacuum Science & Technology A: Vacuum, Surfaces, and Films*, Jg. 34, Nr. 3, S. 31511, 2016, doi: 10.1116/1.4948234.
- [16] C. Fuger *et al.*, „Influence of Tantalum on phase stability and mechanical properties of WB2“, *MRS Communications*, Jg. 9, Nr. 1, S. 375–380, 2019, doi: 10.1557/mrc.2019.5.
- [17] R. Hahn, V. Moraes, A. Limbeck, P. Polcik, P. H. Mayrhofer und H. Euchner, „Electron-configuration stabilized (W,Al)B₂ solid solutions“, *Acta Materialia*, Jg. 174, S. 398–405, 2019, doi: 10.1016/j.actamat.2019.05.056.
- [18] B. Grančič *et al.*, „Stoichiometry, structure and mechanical properties of co-sputtered Ti_{1-x}Ta_xB_{2±Δ} coatings“, *Surface and Coatings Technology*, Jg. 367, S. 341–348, 2019, doi: 10.1016/j.surfcoat.2019.04.017.
- [19] B. Bakhit *et al.*, „Strategy for simultaneously increasing both hardness and toughness in ZrB₂-rich Zr_{1-x}Ta_xB_y thin films“, *Journal of Vacuum Science & Technology A: Vacuum, Surfaces, and Films*, Jg. 37, Nr. 3, S. 31506, 2019, doi: 10.1116/1.5093170.
- [20] M. Magnuson, L. Hultman und H. Högberg, „Review of transition-metal diboride thin films“, *Vacuum*, S. 110567, 2021, doi: 10.1016/j.vacuum.2021.110567.
- [21] P. Kiryukhantsev-Korneev, A. D. Sytchenko, A. Potanin, S. A. Vorotilo und E. A. Levashov, „Mechanical properties and oxidation resistance of Mo-Si-B and Mo-Hf-Si-B coatings obtained by magnetron sputtering in DC and pulsed DC modes“, *Surface and Coatings Technology*, Jg. 403, S. 126373, 2020, doi: 10.1016/j.surfcoat.2020.126373.
- [22] H. Riedl *et al.*, „Thermal stability and mechanical properties of boron enhanced Mo-Si coatings“, *Surface and Coatings Technology*, Jg. 280, S. 282–290, 2015, doi: 10.1016/j.surfcoat.2015.09.015.
- [23] K. G. Budinski, *Friction, Wear, and Erosion Atlas*. Hoboken: Taylor and Francis, 2013. [Online]. Verfügbar unter: <http://gbv.ebib.com/patron/FullRecord.aspx?p=1408045>
- [24] K. Sommer, R. Heinz und J. Schöfer, *Verschleiß metallischer Werkstoffe: Erscheinungsformen sicher beurteilen ; mit zahlreichen Tabellen*, 1. Aufl. Wiesbaden: Vieweg + Teubner, 2010.
- [25] L. Deters, „Tribology“ in *Springer Handbook of Mechanical Engineering*, K.-H. Grote und E. K. Antonsson, Hg., Berlin, Heidelberg: Springer Berlin Heidelberg, 2009, S. 295–326, doi: 10.1007/978-3-540-30738-9_5.
- [26] H. Czichos und K.-H. Habig, *Tribologie-Handbuch*. Wiesbaden: Springer Fachmedien Wiesbaden, 2015.
- [27] L. W. McKeen, *Fatigue and tribological properties of plastics and elastomers*. Amsterdam, Boston, Heidelberg: Elsevier, 2016.
- [28] G. Straffelini, *Friction and Wear: Methodologies for Design and Control*. Cham: Springer, 2015. [Online]. Verfügbar unter: <http://swbplus.bsz-bw.de/bsz430175590cov.htm>
- [29] G. W. Stachowiak, *Wear: Materials, mechanisms and practice*. Chichester, England, Hoboken, NJ: Wiley, 2005. [Online]. Verfügbar unter: <http://search.ebscohost.com/login.aspx?direct=true&scope=site&db=nlebk&db=nlabk&AN=172092>
- [30] E. Bousser, L. Martinu und J. E. Klemberg-Sapieha, „Solid particle erosion mechanisms of hard protective coatings“, *Surface and Coatings Technology*, Jg. 235, S. 383–393, 2013, doi: 10.1016/j.surfcoat.2013.07.050.
- [31] 5.3.1 *Erosion Mechanisms [Aeroengine Safety]*. [Online]. Verfügbar unter: <https://aeroenginesafety.tugraz.at/doku.php?id=5:53:531:531#references> (Zugriff am: 20. Oktober 2021).

- [32] I. Finnie, „Some reflections on the past and future of erosion“, *Wear*, 186-187, S. 1–10, 1995, doi: 10.1016/0043-1648(95)07188-1.
- [33] I. Finnie, „Erosion of surfaces by solid particles“, *Wear*, Jg. 3, Nr. 2, S. 87–103, 1960, doi: 10.1016/0043-1648(60)90055-7.
- [34] A. Khoddami, D. Salimi-Majd und B. Mohammadi, „Finite element and experimental investigation of multiple solid particle erosion on Ti-6Al-4V titanium alloy coated by multilayer wear-resistant coating“, *Surface and Coatings Technology*, Jg. 372, S. 173–189, 2019, doi: 10.1016/j.surfcoat.2019.05.042.
- [35] Etienne Bousser, „Solid Particle Erosion mechanisms of protective coatings for aerospace applications“. Dissertation, Département de genie physique, Université de Montréal, Montréal, 2013.
- [36] C. Maurer, „Versagensmechanismen von PVD-Beschichtungen auf CFK unter Erosionsverschleiß“. Aachen, Techn. Hochsch., Diss., 2014, Hochschulbibliothek der Rheinisch-Westfälischen Technischen Hochschule Aachen, Aachen, 2014. [Online]. Verfügbar unter: <http://darwin.bth.rwth-aachen.de/opus3/volltexte/2014/4975>
- [37] A. Leyland und A. Matthews, „On the significance of the H/E ratio in wear control: a nanocomposite coating approach to optimised tribological behaviour“, *Wear*, Jg. 246, 1-2, S. 1–11, 2000, doi: 10.1016/S0043-1648(00)00488-9.
- [38] *Handbook of sputter deposition technology: Fundamentals and applications for functional thin films, nano-materials and MEMS*, 2. Aufl. Waltham, MA: William Andrew, 2012.
- [39] R. A. Haefer, *Oberflächen- und Dünnschicht-Technologie: Teil I: Beschichtungen von Oberflächen*. Berlin, Heidelberg: Springer, 1987.
- [40] *Magnetron Sputtering Technology Summary | Professor Xiao Research Group* (Zugriff am: 15. Mai 2022).
- [41] J. A. Venables, G. D. T. Spiller und M. Hanbucken, „Nucleation and growth of thin films“, *Rep. Prog. Phys.*, Jg. 47, Nr. 4, S. 399–459, 1984, doi: 10.1088/0034-4885/47/4/002.
- [42] A. Anders, „A structure zone diagram including plasma-based deposition and ion etching“, *Thin Solid Films*, Jg. 518, Nr. 15, S. 4087–4090, 2010, doi: 10.1016/j.tsf.2009.10.145.
- [43] J. A. Thornton, „Influence of apparatus geometry and deposition conditions on the structure and topography of thick sputtered coatings“ (en), *Journal of Vacuum Science and Technology*, Jg. 11, Nr. 4, S. 666–670, 1974, doi: 10.1116/1.1312732.
- [44] R. Messier, A. P. Giri und R. A. Roy, „Revised structure zone model for thin film physical structure“, *Journal of Vacuum Science & Technology A: Vacuum, Surfaces, and Films*, Jg. 2, Nr. 2, S. 500–503, 1984, doi: 10.1116/1.572604.
- [45] *Bor - Chemgapedia*. [Online]. Verfügbar unter: <http://www.chemgapedia.de/vsengine/vlu/vsc/de/ch/16/ac/elemente/vlu/5.vlu.html> (Zugriff am: 30. April 2022).
- [46] GDCh, *Bor: Das fünfte Element – kleiner Nachbar von Kohlenstoff?* [Online]. Verfügbar unter: <https://faszinationchemie.de/wissen-und-fakten/news/bor-das-fuenfte-element-kleiner-nachbar-von-kohlenstoff/> (Zugriff am: 30. April 2022).
- [47] V. Gold, *The IUPAC Compendium of Chemical Terminology*. Research Triangle Park, NC: International Union of Pure and Applied Chemistry (IUPAC), 2019.

- [48] Encyclopedia Britannica, *transition metal* | *Definition, Properties, Elements, & Facts*. [Online]. Verfügbar unter: <https://www.britannica.com/science/transition-metal> (Zugriff am: 30. April 2022).
- [49] M. Mikula *et al.*, „Mechanical properties of superhard TiB₂ coatings prepared by DC magnetron sputtering“, *Vacuum*, Jg. 82, Nr. 2, S. 278–281, 2007, doi: 10.1016/j.vacuum.2007.07.036.
- [50] M. Berger, M. Larsson und S. Hogmark, „Evaluation of magnetron-sputtered TiB₂ intended for tribological applications“, *Surface and Coatings Technology*, Jg. 124, 2-3, S. 253–261, 2000, doi: 10.1016/S0257-8972(99)00638-6.
- [51] P. Villars und H. Okamoto, *B-Ti Binary Phase Diagram 0-100 at.% Ti: Datasheet from “PAULING FILE Multinaries Edition - 2012” in SpringerMaterials* (https://materials.springer.com/isp/phase-diagram/docs/c_0900329). Springer-Verlag Berlin Heidelberg & Material Phases Data System (MPDS), Switzerland & National Institute for Materials Science (NIMS), Japan. Verfügbar unter: https://materials.springer.com/isp/phase-diagram/docs/c_0900329.
- [52] C. Fuger *et al.*, „Revisiting the origins of super-hardness in TiB₂+z thin films – Impact of growth conditions and anisotropy“, *Surface and Coatings Technology*, 2022.
- [53] J. Neidhardt *et al.*, „Experiment and simulation of the compositional evolution of Ti–B thin films deposited by sputtering of a compound target“, *Journal of Applied Physics*, Jg. 104, Nr. 6, S. 63304, 2008, doi: 10.1063/1.2978211.
- [54] B. Hunter *et al.*, „Investigations into the slip behavior of zirconium diboride“, *J. Mater. Res.*, Jg. 31, Nr. 18, S. 2749–2756, 2016, doi: 10.1557/jmr.2016.201.
- [55] C. Fuger *et al.*, „Anisotropic super-hardness of hexagonal WB₂+z thin films“, *Materials Research Letters*, Jg. 10, Nr. 2, S. 70–77, 2022, doi: 10.1080/21663831.2021.2021308.
- [56] S. Guo und H. Sun, „Superhardness Induced by Grain Boundary Vertical Sliding in (001)-textured ZrB₂ and TiB₂ Nano Films“, *Acta Materialia*, Jg. 218, S. 117212, 2021, doi: 10.1016/j.actamat.2021.117212.
- [57] P. Villars und H. Okamoto, *B-Mo Binary Phase Diagram 0-100 at.% Mo: Datasheet from “PAULING FILE Multinaries Edition - 2012” in SpringerMaterials* (https://materials.springer.com/isp/phase-diagram/docs/c_0900299). Springer-Verlag Berlin Heidelberg & Material Phases Data System (MPDS), Switzerland & National Institute for Materials Science (NIMS), Japan. Verfügbar unter: https://materials.springer.com/isp/phase-diagram/docs/c_0900299.
- [58] P. Malinovskis, *Magnetron sputtering of binary, ternary and multicomponent thin film borides and carbides*. Uppsala: Acta Universitatis Upsaliensis, 2018.
- [59] L.-P. Ding *et al.*, „Crystal Structures, Stabilities, Electronic Properties, and Hardness of MoB₂: First-Principles Calculations“ (eng), *Inorganic chemistry*, Jg. 55, Nr. 14, S. 7033–7040, 2016, doi: 10.1021/acs.inorgchem.6b00899.
- [60] L. Zauner *et al.*, „Reactive HiPIMS deposition of Ti-Al-N: Influence of the deposition parameters on the cubic to hexagonal phase transition“, *Surface and Coatings Technology*, Jg. 382, S. 125007, 2020, doi: 10.1016/j.surfcoat.2019.125007.
- [61] A. Ul-Hamid, *A Beginners' Guide to Scanning Electron Microscopy*. Cham: Springer International Publishing, 2018.
- [62] J. Goldstein, D. E. Newbury, J. R. Michael, N. W. M. Ritchie, J. H. J. Scott und D. C. Joy, *Scanning electron microscopy and X-ray microanalysis*. New York, NY, U.S.A.: Springer, 2018.

- [63] *The Transmission Electron Microscope* | CCBER. [Online]. Verfügbar unter: <https://www.ccber.ucsb.edu/ucsb-natural-history-collections-botanical-plant-anatomy/transmission-electron-microscope> (Zugriff am: 2. Mai 2022).
- [64] E. Hornbogen und B. Skrotzki, *Mikro- und Nanoskopie der Werkstoffe*. Berlin, Heidelberg: Springer Berlin Heidelberg, 2009.
- [65] G. M. Pharr und W. C. Oliver, „Measurement of Thin Film Mechanical Properties Using Nanoindentation“, *MRS Bull.*, Jg. 17, Nr. 7, S. 28–33, 1992, doi: 10.1557/S0883769400041634.
- [66] A. C. Fischer-Cripps, „Critical review of analysis and interpretation of nanoindentation test data“, *Surface and Coatings Technology*, Jg. 200, 14-15, S. 4153–4165, 2006, doi: 10.1016/j.surfcoat.2005.03.018.
- [67] *Erzeugung von RÖNTGEN-Strahlung* | LEIFIPhysik. [Online]. Verfügbar unter: <https://www.leifiphysik.de/atomphysik/roentgen-strahlung/grundwissen/erzeugung-von-roentgen-strahlung> (Zugriff am: 1. Mai 2022).
- [68] *Moderne Röntgenbeugung: Röntgendiffraktometrie für Materialwissenschaftler, Physiker und Chemiker*, 2. Aufl. Wiesbaden: Vieweg + Teubner, 2009.
- [69] J. Rösler, H. Harders und M. Bäker, *Mechanisches Verhalten der Werkstoffe*, 6. Aufl. Wiesbaden: Springer Vieweg, 2019.
- [70] H. A. Richard, *Ermüdungsrisse: Erkennen, sicher beurteilen, vermeiden*. Wiesbaden: Vieweg+Teubner, 2009.
- [71] J. Ast, M. Ghidelli, K. Durst, M. Göken, M. Sebastiani und A. M. Korsunsky, „A review of experimental approaches to fracture toughness evaluation at the micro-scale“, *Materials & Design*, Jg. 173, S. 107762, 2019, doi: 10.1016/j.matdes.2019.107762.
- [72] D. Di Maio und S. G. Roberts, „Measuring fracture toughness of coatings using focused-ion-beam-machined microbeams“, *J. Mater. Res.*, Jg. 20, Nr. 2, S. 299–302, 2005, doi: 10.1557/JMR.2005.0048.
- [73] K. Matoy *et al.*, „A comparative micro-cantilever study of the mechanical behavior of silicon based passivation films“, *Thin Solid Films*, Jg. 518, Nr. 1, S. 247–256, 2009, doi: 10.1016/j.tsf.2009.07.143.
- [74] J. R. Laguna-Camacho, L. A. Cruz-Mendoza, J. C. Anzelmetti-Zaragoza, A. Marquina-Chávez, M. Vite-Torres und J. Martínez-Trinidad, „Solid particle erosion on coatings employed to protect die casting molds“, *Progress in Organic Coatings*, Jg. 74, Nr. 4, S. 750–757, 2012, doi: 10.1016/j.porgcoat.2011.09.022.
- [75] M. Weiss, H. Riedl, V. Moares, P. H. Mayrhofer und A. Limbeck, „Laser based analysis of transition metal boride thin films using liquid standards“, *Microchemical Journal*, Jg. 152, S. 104449, 2020, doi: 10.1016/j.microc.2019.104449.
- [76] M. Bartosik, C. Rumeau, R. Hahn, Z. L. Zhang und P. H. Mayrhofer, „Fracture toughness and structural evolution in the TiAlN system upon annealing“ (eng), *Scientific reports*, Jg. 7, Nr. 1, S. 16476, 2017, doi: 10.1038/s41598-017-16751-1.